Strange particle production in $p + p$ collisions at $\sqrt{s} = 200$ GeV

B. I. Abelev,[50] J. Adams,[2] M. M. Aggarwal,[30] Z. Ahammed,[45] J. Amonett,[20] B. D. Anderson,[20] M. Anderson,[6] D. Arkhipkin,[13] G. S. Averichev,[12] Y. Bai,[28] J. Balewski,[17] O. Barannikova,[9] L. S. Barnby,[2] J. Baudot,[18] S. Bekele,[29] V. V. Belaga,[12] A. Bellingeri-Laurikainen,[40] R. Bellwied,[48] F. Benedosso,[28] S. Bhardwaj,[35] A. Bhasin,[19] A. K. Bhati,[30] H. Bichsel,[47] J. Bielcik,[50] J. Bielcikova,[50] L. C. Bland,[3] S.-L. Blyth,[22] B. E. Bonner,[36] M. Botje,[28] J. Bouchet,[40] A. V. Brandin,[26] A. Bravar,[3] T. P. Burton,[2] M. Bystersky,[11] R. V. Cadman,[1] X. Z. Cai,[39] H. Caines,[50] M. Calderón de la Barca Sánchez,[6] J. Castillo,[28] O. Catu,[50] D. Cebra,[6] Z. Chajecki,[29] P. Chaloupka,[11] S. Chattopadhyay,[45] H. F. Chen,[38] J. H. Chen,[39] J. Cheng,[43] M. Cherney,[10] A. Chikanian,[50] W. Christie,[3] J. P. Coffin,[18] T. M. Cormier,[48] M. R. Cosentino,[37] J. G. Cramer,[47] H. J. Crawford,[5] D. Das,[45] S. Das,[45] S. Dash,[15] M. Daugherity,[42] M. M. de Moura,[37] T. G. Dedovich,[12] M. DePhillips,[3] A. A. Derevschikov,[32] L. Didenko,[3] T. Dietel,[14] P. Djawotho,[17] S. M. Dogra,[19] W. J. Dong,[7] X. Dong,[38] J. E. Draper,[6] F. Du,[50] V. B. Dunin,[12] J. C. Dunlop,[3] M. R. Dutta Mazumdar,[45] V. Eckardt,[24] W. R. Edwards,[22] L. G. Efimov,[12] V. Emelianov,[26] J. Engelage,[5] G. Eppley,[36] B. Erazmus,[40] M. Estienne,[18] P. Fachini,[3] R. Fatemi,[23] J. Fedorisin,[12] K. Filimonov,[22] P. Filip,[13] E. Finch,[50] V. Fine,[3] Y. Fisyak,[3] J. Fu,[49] C. A. Gagliardi,[41] L. Gaillard,[2] M. S. Ganti,[45] V. Ghazikhanian,[7] P. Ghosh,[45] J. E. Gonzalez,[7] Y. G. Gorbunov,[10] H. Gos,[46] O. Grebenyuk,[28] D. Grosnick,[44] S. M. Guertin,[7] K. S. F. F. Guimaraes,[37] A. Gupta,[19] T. D. Gutierrez,[6] B. Haag,[6] T. J. Hallman,[3] A. Hamed,[48] J. W. Harris,[50] W. He,[17] M. Heinz,[50] T. W. Henry,[41] S. Hepplemann,[31] B. Hippolyte,[18] A. Hirsch,[33] E. Hjort,[22] A. M. Hoffman,[23] G. W. Hoffmann,[42] M. J. Horner,[22] H. Z. Huang,[7] S. L. Huang,[38] E. W. Hughes,[4] T. J. Humanic,[29] G. Igo,[7] P. Jacobs,[22] W. W. Jacobs,[17] P. Jakl,[11] F. Jia,[21] H. Jiang,[7] P. G. Jones,[2] E. G. Judd,[5] S. Kabana,[40] K. Kang,[43] J. Kapitan,[11] M. Kaplan,[8] D. Keane,[20] A. Kechechyan,[12] V. Yu. Khodyrev,[32] B. C. Kim,[34] J. Kiryluk,[23] A. Kisiel,[46] E. M. Kislov,[12] S. R. Klein,[22] A. Kocoloski,[23] D. D. Koetke,[44] T. Kollegger,[14] M. Kopytine,[20] L. Kotchenda,[26] V. Kouchpil,[11] K. L. Kowalik,[22] M. Kramer,[27] P. Kravtsov,[26] V. I. Kravtsov,[32] K. Krueger,[1] C. Kuhn,[18] A. I. Kulikov,[12] A. Kumar,[30] A. A. Kuznetsov,[12] M. A. C. Lamont,[50] J. M. Landgraf,[3] S. Lange,[14] S. LaPointe,[48] F. Laue,[3] J. Lauret,[3] A. Lebedev,[3] R. Lednicky,[13] C.-H. Lee,[34] S. Lehocka,[12] M. J. LeVine,[3] C. Li,[38] Q. Li,[48] Y. Li,[43] G. Lin,[50] X. Lin,[49] S. J. Lindenbaum,[27] M. A. Lisa,[29] F. Liu,[49] H. Liu,[38] J. Liu,[36] L. Liu,[49] Z. Liu,[49] T. Ljubicic,[3] W. J. Llope,[36] H. Long,[7] R. S. Longacre,[3] W. A. Love,[3] Y. Lu,[49] T. Ludlam,[3] D. Lynn,[3] G. L. Ma,[39] J. G. Ma,[7] Y. G. Ma,[39] D. Magestro,[29] D. P. Mahapatra,[15] R. Majka,[50] L. K. Mangotra,[19] R. Manweiler,[44] S. Margetis,[20] C. Markert,[42] L. Martin,[40] H. S. Matis,[22] Yu. A. Matulenko,[32] C. J. McClain,[1] T. S. McShane,[10] Yu. Melnick,[32] A. Meschanin,[32] J. Millane,[23] M. L. Miller,[23] N. G. Minaev,[32] S. Mioduszewski,[41] C. Mironov,[20] A. Mischke,[28] D. K. Mishra,[15] J. Mitchell,[36] B. Mohanty,[45] L. Molnar,[33] C. F. Moore,[42] D. A. Morozov,[32] M. G. Munhoz,[37] B. K. Nandi,[16] C. Nattrass,[50] T. K. Nayak,[45] J. M. Nelson,[2] P. K. Netrakanti,[45] L. V. Nogach,[32] S. B. Nurushev,[32] G. Odyniec,[22] A. Ogawa,[3] V. Okorokov,[26] M. Oldenburg,[22] D. Olson,[22] M. Pachr,[11] S. K. Pal,[45] Y. Panebratsev,[12] S. Y. Panitkin,[3] A. I. Pavlinov,[48] T. Pawlak,[46] T. Peitzmann,[28] V. Perevoztchikov,[3] C. Perkins,[5] W. Peryt,[46] S. C. Phatak,[15] R. Picha,[6] M. Planinic,[51] J. Pluta,[46] N. Poljak,[51] N. Porile,[33] J. Porter,[47] A. M. Poskanzer,[22] M. Potekhin,[3] E. Potrebenikova,[12] B. V. K. S. Potukuchi,[19] D. Prindle,[47] C. Pruneau,[48] J. Putschke,[22] G. Rakness,[31] R. Raniwala,[35] S. Raniwala,[35] R. L. Ray,[42] S. V. Razin,[12] J. Reinnarth,[40] D. Relyea,[4] F. Retiere,[22] A. Ridiger,[26] H. G. Ritter,[22] J. B. Roberts,[36] O. V. Rogachevskiy,[12] J. L. Romero,[6] A. Rose,[22] C. Roy,[40] L. Ruan,[22] M. J. Russcher,[28] R. Sahoo,[15] T. Sakuma,[23] S. Salur,[50] J. Sandweiss,[50] M. Sarsour,[41] P. S. Sazhin,[12] J. Schambach,[42] R. P. Scharenberg,[33] N. Schmitz,[24] K. Schweda,[22] J. Seger,[10] I. Selyuzhenkov,[48] P. Seyboth,[24] A. Shabetai,[20] E. Shahaliev,[12] M. Shao,[38] M. Sharma,[30] W. Q. Shen,[39] S. S. Shimanskiy,[12] E. Sichtermann,[22] F. Simon,[23] R. N. Singaraju,[45] N. Smirnov,[50] R. Snellings,[28] G. Sood,[44] P. Sorensen,[3] J. Sowinski,[17] J. Speltz,[18] H. M. Spinka,[1] B. Srivastava,[33] A. Stadnik,[12] T. D. S. Stanislaus,[44] R. Stock,[14] A. Stolpovsky,[48] M. Strikhanov,[26] B. Stringfellow,[33] A. A. P. Suaide,[37] E. Sugarbaker,[29] M. Sumbera,[11] Z. Sun,[21] B. Surrow,[23] M. Swanger,[10] T. J. M. Symons,[22] A. Szanto de Toledo,[37] A. Tai,[7] J. Takahashi,[37] A. H. Tang,[3] T. Tarnowsky,[33] D. Thein,[7] J. H. Thomas,[22] A. R. Timmins,[2] S. Timoshenko,[26] M. Tokarev,[12] T. A. Trainor,[47] S. Trentalange,[7] R. E. Tribble,[41] O. D. Tsai,[7] J. Ulery,[33] T. Ullrich,[3] D. G. Underwood,[1] G. Van Buren,[3] N. van der Kolk,[28] M. van Leeuwen,[22] A. M. Vander Molen,[25] R. Varma,[16] I. M. Vasilevski,[13] A. N. Vasiliev,[32] R. Vernet,[18] S. E. Vigdor,[17] V. P. Viyogi,[15] S. Vokal,[12] S. A. Voloshin,[48] W. T. Waggoner,[10] F. Wang,[33] G. Wang,[7] J. S. Wang,[21] X. L. Wang,[38] Y. Wang,[43] J. W. Watson,[20] J. C. Webb,[44] G. D. Westfall,[25] A. Wetzler,[22] C. Whitten Jr.,[7] H. Wieman,[22] S. W. Wissink,[17] R. Witt,[50] J. Wood,[7] J. Wu,[38] N. Xu,[22] Q. H. Xu,[22] Z. Xu,[3] P. Yepes,[36] I.-K. Yoo,[34] V. I. Yurevich,[12] W. Zhan,[21] H. Zhang,[3] W. M. Zhang,[20] Y. Zhang,[38] Z. P. Zhang,[38] Y. Zhao,[38] C. Zhong,[39] R. Zoulkarneev,[13] Y. Zoulkarneeva,[13] A. N. Zubarev,[12] and J. X. Zuo[39]

(STAR Collaboration)

[1]*Argonne National Laboratory, Argonne, Illinois 60439, USA*
[2]*University of Birmingham, Birmingham, United Kingdom*
[3]*Brookhaven National Laboratory, Upton, New York 11973, USA*
[4]*California Institute of Technology, Pasadena, California 91125, USA*
[5]*University of California, Berkeley, California 94720, USA*
[6]*University of California, Davis, California 95616, USA*
[7]*University of California, Los Angeles, California 90095, USA*
[8]*Carnegie Mellon University, Pittsburgh, Pennsylvania 15213, USA*
[9]*University of Illinois, Chicago, Illinois, USA*

[10]*Creighton University, Omaha, Nebraska 68178, USA*
[11]*Nuclear Physics Institute AS CR, 250 68 Řež/Prague, Czech Republic*
[12]*Laboratory for High Energy (JINR), Dubna, Russia*
[13]*Particle Physics Laboratory (JINR), Dubna, Russia*
[14]*University of Frankfurt, Frankfurt, Germany*
[15]*Institute of Physics, Bhubaneswar 751005, India*
[16]*Indian Institute of Technology, Mumbai, India*
[17]*Indiana University, Bloomington, Indiana 47408, USA*
[18]*Institut de Recherches Subatomiques, Strasbourg, France*
[19]*University of Jammu, Jammu 180001, India*
[20]*Kent State University, Kent, Ohio 44242, USA*
[21]*Institute of Modern Physics, Lanzhou, People's Republic of China*
[22]*Lawrence Berkeley National Laboratory, Berkeley, California 94720, USA*
[23]*Massachusetts Institute of Technology, Cambridge, Massachusetts 02139-4307, USA*
[24]*Max-Planck-Institut für Physik, Munich, Germany*
[25]*Michigan State University, East Lansing, Michigan 48824, USA*
[26]*Moscow Engineering Physics Institute, Moscow Russia*
[27]*City College of New York, New York City, New York 10031, USA*
[28]*NIKHEF and Utrecht University, Amsterdam, The Netherlands*
[29]*Ohio State University, Columbus, Ohio 43210, USA*
[30]*Panjab University, Chandigarh 160014, India*
[31]*Pennsylvania State University, University Park, Pennsylvania 16802, USA*
[32]*Institute of High Energy Physics, Protvino, Russia*
[33]*Purdue University, West Lafayette, Indiana 47907, USA*
[34]*Pusan National University, Pusan, Republic of Korea*
[35]*University of Rajasthan, Jaipur 302004, India*
[36]*Rice University, Houston, Texas 77251, USA*
[37]*Universidade de Sao Paulo, Sao Paulo, Brazil*
[38]*University of Science & Technology of China, Hefei 230026, People's Republic of China*
[39]*Shanghai Institute of Applied Physics, Shanghai 201800, People's Republic of China*
[40]*SUBATECH, Nantes, France*
[41]*Texas A&M University, College Station, Texas 77843, USA*
[42]*University of Texas, Austin, Texas 78712, USA*
[43]*Tsinghua University, Beijing 100084, People's Republic of China*
[44]*Valparaiso University, Valparaiso, Indiana 46383, USA*
[45]*Variable Energy Cyclotron Centre, Kolkata 700064, India*
[46]*Warsaw University of Technology, Warsaw, Poland*
[47]*University of Washington, Seattle, Washington 98195, USA*
[48]*Wayne State University, Detroit, Michigan 48201, USA*
[49]*Institute of Particle Physics, CCNU (HZNU), Wuhan 430079, People's Republic of China*
[50]*Yale University, New Haven, Connecticut 06520, USA*
[51]*University of Zagreb, Zagreb, HR-10002, Croatia*

(Received 2 August 2006; published 4 June 2007)

We present strange particle spectra and yields measured at midrapidity in $\sqrt{s} = 200$ GeV proton-proton ($p + p$) collisions at the BNL Relativistic Heavy Ion Collider (RHIC). We find that the previously observed universal transverse mass ($m_T \equiv \sqrt{{p_T}^2 + m^2}$) scaling of hadron production in $p + p$ collisions seems to break down at higher m_T and that there is a difference in the shape of the m_T spectrum between baryons and mesons. We observe midrapidity antibaryon to baryon ratios near unity for Λ and Ξ baryons and no dependence of the ratio on transverse momentum, indicating that our data do not yet reach the quark-jet dominated region. We show the dependence of the mean transverse momentum $\langle p_T \rangle$ on measured charged particle multiplicity and on particle mass and infer that these trends are consistent with gluon-jet dominated particle production. The data are compared with previous measurements made at the CERN Super Proton Synchrotron and Intersecting Storage Rings and in Fermilab experiments and with leading-order and next-to-leading-order string fragmentation model predictions. We infer from these comparisons that the spectral shapes and particle yields from $p + p$ collisions at RHIC energies have large contributions from gluon jets rather than from quark jets.

DOI: 10.1103/PhysRevC.75.064901 PACS number(s): 25.75.Dw, 25.40.Ep

I. INTRODUCTION

The production of particles in elementary proton-proton ($p + p$) collisions is thought to be governed by two mechanisms. Namely, soft, thermal-like processes which populate the low momentum part of the particle spectra (the so-called underlying event) and the hard parton-parton interaction process. In this scenario, the low transverse momentum (p_T) part of the spectrum is exponential in transverse mass ($m_T \equiv \sqrt{m^2 + p_T{}^2}$); while fragmentation, in leading-order models, introduces a power-law tail at high p_T. We investigate the validity of these assumptions at energies currently available at the BNL Relativistic Heavy Ion Collider (RHIC) by studying the spectral shapes and the yields of identified strange hadron spectra from the lightest strange mesons ($K^{\pm}$) to the heavy, triply strange Ω^- baryon.

In this paper, we report the results for transverse momentum spectra and midrapidity yields (dN/dy) of $K^{\pm}$, K^0_S, Λ, $\overline{\Lambda}$, Ξ^-, $\overline{\Xi}^+$, and $\Omega^- + \overline{\Omega}^+$ measured by the STAR experiment during the 2001–2002 $\sqrt{s} = 200$ GeV $p + p$ running at RHIC. After a brief description in Sec. II of the experimental setup and conditions for this run, we describe in Sec. III A the event selection criteria and efficiency of reconstructing the primary interaction vertex. Specific attention is given to the complications introduced by more than one event occurring in the detector during readout, a condition referred to as "pileup." The details of strange particle reconstruction and the efficiency thereof will be discussed in Secs. III B, III C, and III D. In Sec. IV A we describe the final measured p_T spectra and midrapidity yields. We also describe the functions used to parametrize the p_T spectra in order to extrapolate the measurement to zero p_T. We will show that the previously widely used power-law extrapolation for $p + p$ and $p + \overline{p}$ collisions [1] does not yield the best χ^2 results for the strange baryons, and we will consider alternatives. Section IV B introduces the idea of transverse mass scaling (m_T scaling) and its applicability to our data. The measured antiparticle to particle ratios are presented in Sec. IV C. Interesting trends of increasing mean transverse momentum, $\langle p_T \rangle$, with particle mass have been previously observed in $p + p$ collisions at energies currently available at the CERN Intersecting Storage Rings (ISR) ($20 \leqslant \sqrt{s} \leqslant 63$ GeV) [2]. Mean transverse momentum has also been found to increase with event multiplicity in $p + \overline{p}$ collisions at energies available at the CERN Super Proton-Antiproton Synchrotron (S$p\overline{p}$S) ($\sqrt{s} =$ 630 GeV) [1] and at Fermilab (300 GeV $\leqslant \sqrt{s} \leqslant 1.8$ TeV) [3,4]. We will show the dependence of our $\langle p_T \rangle$ measurements on both particle mass and event multiplicity in Sec. IV D. We discuss the details of the experimental errors and then compare our results in Sec. V with several models that attempt to describe particle production in $p + p$ collisions via pQCD, string fragmentation, and minijets [5]. We conclude in Sec. VI with a discussion of the major results and some remarks about future directions for the ongoing analyses.

II. EXPERIMENTAL SETUP

The data presented in this paper were collected with the Solenoidal Tracker at RHIC (STAR) detector [6]. The primary detector subsystem used for these analyses is the large cylindrical time projection chamber (TPC), which is able to track charged particles in the pseudorapidity range $|\eta| \leqslant 1.8$ with full azimuthal coverage [7]. The TPC has 45 pad rows in the radial direction, allowing a maximum of 45 hits to be located on a given charged particle track. A uniform magnetic field of 0.5 T is applied along the beamline by the surrounding solenoidal coils, allowing the momentum of charged particles to be determined to within 2–7% depending on the transverse momentum of the particle. The field polarity was reversed once during the 2001–2002 run to allow for studies of systematic errors. The TPC tracking efficiency in $p + p$ collisions is greater than 90% for charged particles with $p_T \geqslant 300$ MeV/c in the pseudorapidity region $|\eta| < 0.7$ [7]. Particle identification may be achieved via measurements of energy loss due to specific ionization from charged particles passing through the TPC gas (dE/dx). The dE/dx, when plotted vs rigidity separates the tracks into several bands which depend on the particle mass. A semiempirical formula describing the variation of dE/dx with rigidity is provided by the Bethe-Bloch equation [8]. An updated form, which accounts for the path length of a given particle through matter, has been given by Bichsel and provides a reasonable description of the dE/dx band centers for the particles presented in this paper [8]. The Bichsel curves are shown in Fig. 1.

The dataset analyzed in this paper consisted of 1.4×10^7 minimally biased events before cuts. After applying a cut requiring the location of the primary vertex to be within 50 cm of the center of the TPC along the beam axis, to limit acceptance variations, 6×10^6 events remained. In all events, the detectors were triggered by requiring the simultaneous detection of at least one charged particle at forward rapidities ($3.5 \leqslant |\eta| \leqslant 5.0$) in beam-beam scintillating counters (BBCs) located at both ends of the TPC. This is referred to as a minimally biased trigger. The BBCs are sensitive only to the non-singly-diffractive (NSD) part (30 mb) of the $p + p$ total inelastic cross section (42 mb) [9,10]. A more detailed description of STAR in general [6] and the complete details of the TPC in particular [7] can be found elsewhere.

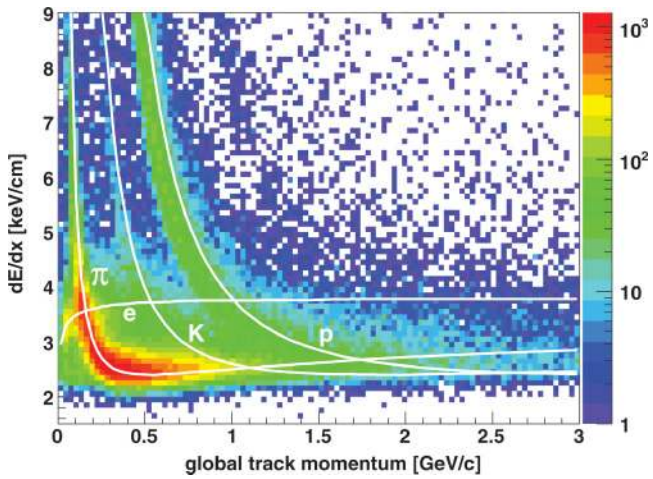

FIG. 1. (Color online) dE/dx vs momentum for STAR $p + p$ collisions at $\sqrt{s} = 200$ GeV. The curves are Bichsel parametrizations [8].

III. ANALYSIS

A. Primary vertex finding and event selection

The position of the interaction vertex is calculated by considering only those tracks which can be matched to struck slats of the STAR central trigger barrel (CTB) [11]. The CTB is a scintillating detector coarsely segmented into 240 slats placed azimuthally around the outside of the STAR TPC at a radius of 2 m. It has a total pseudorapidity coverage of $-1.0 < \eta < 1.0$ and has a fast response time of 10–60 ns, which is roughly one-quarter of the time between beam bunch crossings (218 ns in the 2001–2002 run). Therefore, in approximately 95.6% of our $p + p$ collisions, only charged particles from the triggered event will produce signals in the CTB, which ensures that the primary vertex is initiated with tracks from the triggered event only (note that unlike the BBCs, the CTB itself is not used as a trigger detector for the event sample presented here). Furthermore, the primary vertex is assumed to be located somewhere along the known beamline. The z coordinate (along the beam) of the primary vertex is then determined by minimizing the χ^2 of the distance of closest approach of the tracks to the primary vertex.

The RHIC beams were tuned so as to maximize the luminosity and, consequently, the number of collisions that can be recorded. The average RHIC luminosities, which varied from 5×10^{28} to $5 \times 10^{30}\text{cm}^{-2}\text{s}^{-1}$, produce collisions more frequently (on the order of 2–200 kHz) than the TPC can be read out (100 Hz). During $p + p$ running, as many as five pileup events can overlap (coming in the $\sim 39\,\mu$s before or after an event trigger) in the volume of the TPC. Pileup events come earlier or later than the event trigger, and tracks from pileup events may therefore be only partially reconstructed as track fragments. These track fragments from a pileup event can distort the determination of the location of the primary interaction vertex, as they do not point back to the vertex of the triggered event. To solve this problem, tracks that do not match to a struck CTB slat are not used in the determination of the primary vertex position. The remaining pileup tracks, which match by chance to fired CTB slats, can then be removed with a reasonably restrictive (2–3 cm) analysis cut on a track's distance of closest approach to the determined primary vertex.

Another problem faced in the event reconstruction is the observation that for many minimally biased triggers, no primary vertex is reconstructed. The problem is systematically worse for the low multiplicity events. Therefore, a correction must be applied to account for the events that are triggered on yet lost in the analyses due to an unreconstructed primary vertex.

The efficiency of the primary vertex finding software was investigated by generating Monte Carlo (MC) $p + p$ events, propagating the Monte Carlo produced particles through the STAR detector simulation (GEANT), then adding the resulting simulated signals into the abort-gap events. In an abort-gap event, the detectors are intentionally triggered when there are no protons in one or both of the beam bunches passing through the detector. Abort-gap events therefore contain background due to the interaction of beam particles with remnant gas in the beampipe and may also contain background remaining in the TPC from collisions in the crossings of previous or subsequent beam bunches. Abort-gap events provide a realistic background environment in which to simulate the vertex finding process. The embedded simulated event is then passed through the full software chain, and tracks are reconstructed. These events are then compared with the input from the MC events. A quantity $\Delta(z)$, representing the difference along the z (beam) axis between the actual embedded MC primary vertex (PV) and the reconstructed primary vertex is defined as

$$\Delta(z) = \left| z_{\text{PV}}^{\text{MC}} - z_{\text{PV}}^{\text{reconstructed}} \right|. \tag{1}$$

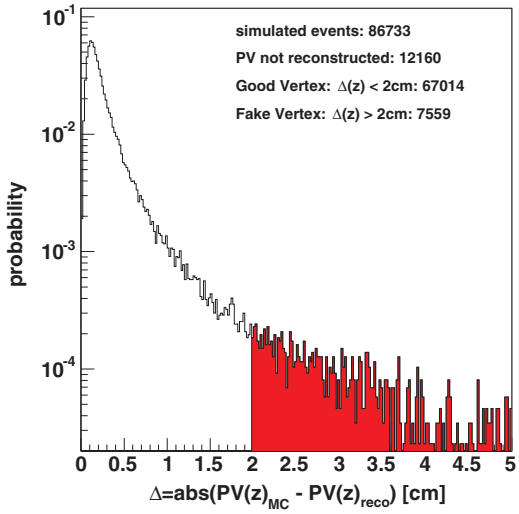

FIG. 2. (Color online) Distribution of $\Delta(z)$. Unshaded region is the accepted range of good reconstructed event vertices.

The probability distribution of $\Delta(z)$ is shown in Fig. 2 for approximately 87 000 simulated events. We separate events in which the software finds a vertex into two classes. An event with a good primary vertex is defined as having $\Delta(z) \leqslant 2$ cm, whereas a fake vertex event is one in which $\Delta(z) > 2$ cm. While this limiting value is somewhat arbitrary, it does relate to offline cuts in our particle reconstruction that are sensitive to the accuracy of the found vertex.

It was found that the probability of finding the primary vertex was strongly dependent on multiplicity. For the purposes of this study, "charged track multiplicity" is defined as being a count of tracks in the TPC that have at least 15 hits, at least 10 of which must be used in the track fit. After separating the raw charged track multiplicity distributions for each event class, i.e., lost vertex, fake vertex, and good vertex, these distributions can be divided by the charged track multiplicity distribution of all events. This ratio then represents the probability for a certain event class to occur as a function of the measured charged track event multiplicity. Finally, the probabilities for each charged track multiplicity are mapped back to the corresponding primary track multiplicity, where "primary tracks" are those which satisfy the above requirements and additionally point back to within 3 cm of the primary vertex. The probabilities for each event class as a function of primary track multiplicity are shown in Fig. 3. Whereas lost vertex events are monotonically decreasing with increasing multiplicity, fake vertex events are most

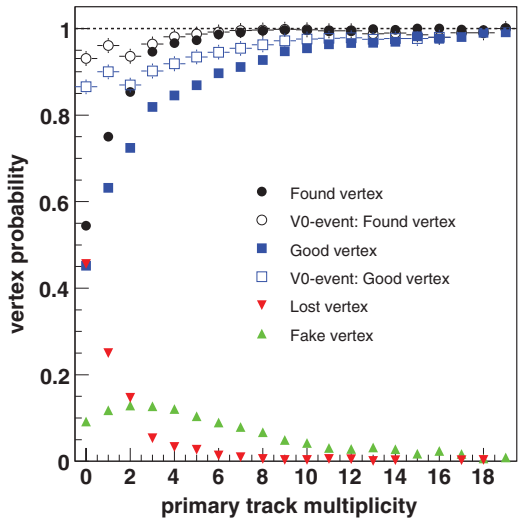

FIG. 3. (Color online) Primary vertex finding efficiency vs measured primary track multiplicity. Horizontal line at unity is only a guide for the eye.

probable when the event has two primary tracks. The open symbols in Fig. 3 show the corresponding "found" and "good" probabilities for events that contained at least one V0 candidate (V0 is explained below). Note that primary vertex finding is initiated with tracks pointing at fired slats of the CTB, as mentioned above. But all found tracks are allowed to contribute to the final vertex position. Therefore, on rare occasions and in low multiplicity events, a vertex may be found with no single track pointing back within 3 cm. These events will appear in Fig. 3 as having a found (or fake) vertex but zero primary track multiplicity. The use of these probabilities to correct the strange particle yields and event counts as a function of multiplicity is described later.

B. Particle identification

All the strange particles presented here, with the exception of the charged kaons, were identified from the topology of their weak decay products in the dominant channel:

$$\mathrm{K}^0_S \rightarrow \pi^+ + \pi^- \ (68.6\%), \tag{2}$$

$$\Lambda \rightarrow p + \pi^- \ (63.9\%), \tag{3}$$

$$\Xi^- \rightarrow \Lambda + \pi^- \ (99.9\%), \tag{4}$$

$$\Omega^- \rightarrow \Lambda + K^- \ (67.8\%). \tag{5}$$

The charged tracks of the daughters of neutral strange particle decays form a characteristic V-shaped topological pattern known as a V0. The V0 finding software pairs oppositely charged particle tracks to form V0 candidates. These candidates can then be further paired with a single charged track, referred to as the "bachelor" to form candidates for Ξ^- and Ω decays. During the initial finding process, loose cuts are applied to partially reduce the background while maximizing the candidate pool. Once the candidate pool is assembled, a more stringent set of cuts is applied to maximize the signal-to-noise ratio and ensure the quality of the sample. The cuts are analysis dependent and are summarized in Table I for the K^0_S and Λ analyses and in Table II for the Ξ and Ω analyses.

TABLE I. Summary of K^0_S and Λ cuts. Candidates that do not satisfy the tabulated requirements are removed from the data sample.

Cut	K^0_S	Λ and $\overline{\Lambda}$
DCA of V0 to primary vertex	<2.0 cm	<2.0 cm
DCA of V0 daughters	<0.9 cm	<0.9 cm
N(hits) daughters	>14	>14
$N(\sigma)\, dE/dx$	<3	<5
Radial decay length	>2.0 cm	>2.0 cm
Parent rapidity (y)	$\pm$0.5	$\pm$0.5

Several of these cuts require some further explanation. A correlation has been observed between the luminosity and the raw V0 multiplicity. This correlation is suggestive of pileup events producing secondary V0s, a contamination estimated to be approximately 18% of the measured yield. The apparent path of the V0 parent particle (the K^0_S or Λ) is extrapolated back toward the primary vertex. The distance of closest approach (DCA) of the V0 parent to the primary vertex is then determined. Secondary V0s from pileup events do not point back well to the primary vertex of the triggered event and may therefore be removed via a cut on the DCA of the V0 parent to the primary vertex. We estimate a remaining contamination of 6% after the cut is applied. Parent particles for secondary V0s may be charged and curve away from the primary vertex before decaying, causing the secondary V0 to also point back poorly. Therefore, this cut also removes some true secondary V0s.

Tracks in the TPC are occasionally broken into two or more segments that appear to be independent tracks to the V0 and Ξ finding software. In the majority of cases, this is due to tracks

TABLE II. Summary of Ξ and Ω cuts. Candidates that do not satisfy the tabulated requirements are removed from the data sample.

Cut	Ξ^- and $\overline{\Xi}^+$	Ω^- and $\overline{\Omega}^+$
Hyperon inv. mass	1321 $\pm$ 5 MeV	1672 $\pm$ 5 MeV
Daughter Λ inv. mass	1115 $\pm$ 5 MeV	1115 $\pm$ 5 MeV
$N(\sigma)\, dE/dx$ bachelor	<5	<3
$N(\sigma)\, dE/dx$ pos. daugh.	<5	<3.5
$N(\sigma)\, dE/dx$ neg. daugh.	<5	<3.5
N(hits) bachelor	>14	>14
N(hits) pos. daugh.	>14	>14
N(hits) neg. daugh.	>14	>14
Parent decay length (lower)	>2.0 cm	>1.25 cm
Parent decay length (upper)	<20 cm	<30 cm
Daugh. V0 decay length (lower)	N/A	>0.5 cm
Daugh. V0 decay length (upper)	N/A	<30 cm
DCA of parent to PV	N/A	<1.2 cm
DCA of daughters	N/A	<0.8 cm
DCA of V0 Daughters	N/A	<0.8 cm
DCA of bchelor to PV (lower)	N/A	>0.5 cm
DCA of bachelor to PV (upper)	N/A	<30 cm
Parent rapidity	$\pm$0.5	$\pm$0.5

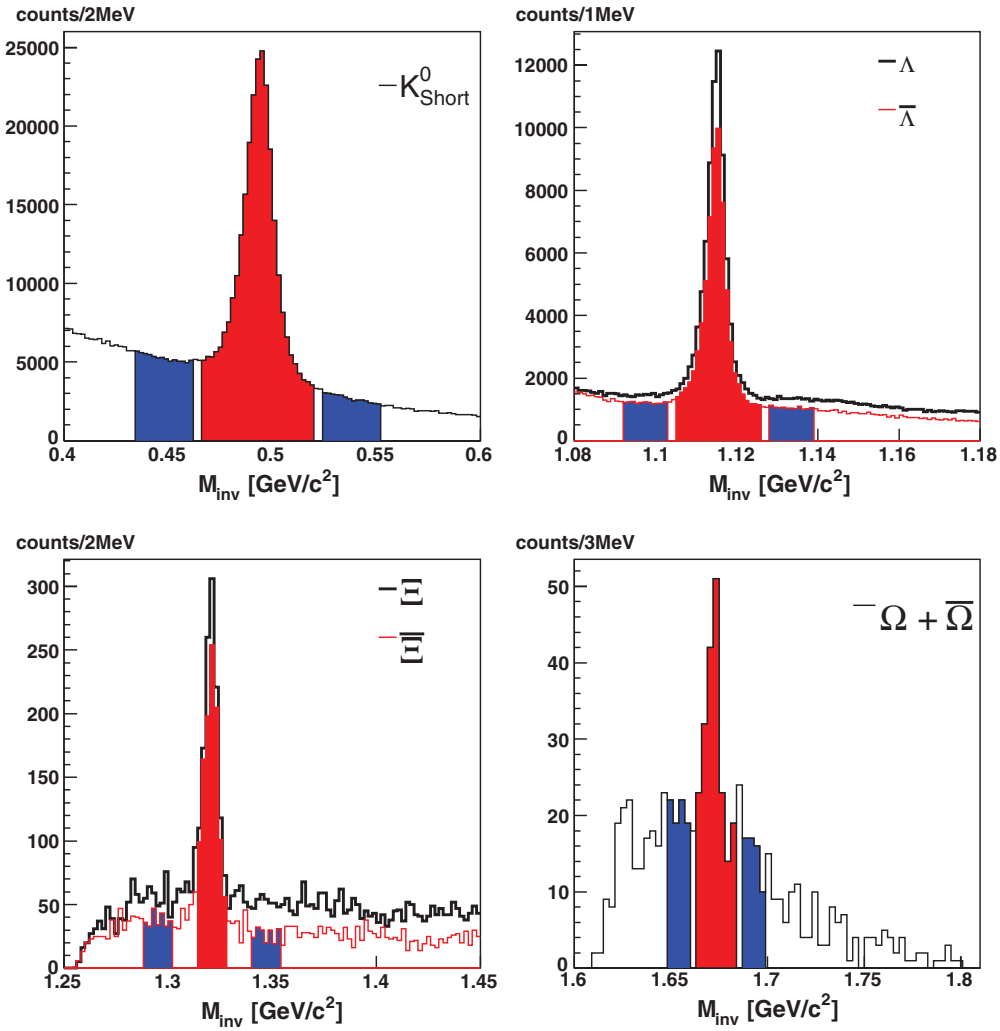

FIG. 4. (Color online) Invariant mass distribution of K^0_S, Λ, $\overline{\Lambda}$, Ξ^-, $\overline{\Xi}^+$, and $\Omega^- + \overline{\Omega}^+$ after applying the geometrical cuts outlined in Tables I and II.

crossing the boundaries between sectors of the TPC pad plane. A cut requiring a minimum number of hits is applied to each of the decay daughter tracks to minimize the contamination from these track fragments.

We also define a variable $N(\sigma)$ to quantitatively measure the residual of a particular track to a certain particle band in dE/dx vs rigidity space [12,13]:

$$N(\sigma) = \frac{dE/dx_{\text{measured}} - dE/dx_{\text{Bichsel}}}{(R/\sqrt{N_{\text{samples}}})(dE/dx_{\text{measured}})}, \tag{6}$$

where R is the dE/dx resolution (width in dE/dx of the distribution of a given particle band, see Fig. 1) at the track's momentum, and N_{samples} is the number of hits used in the determination of the dE/dx. $N(\sigma)$ is therefore inversely proportional to the probability of a particle track matching a given identity. Cutting on the $N(\sigma)$ of a given track helps to decrease the background even further by decreasing the contamination of the candidate pool due to misidentified tracks. This is particularly important for the Ω analysis. The Λ and Ξ analyses can tolerate more open cuts in favor of increased statistics. The invariant mass distributions for K^0_S, Λ, Ξ^-, Ω, and their corresponding antiparticles are shown in Fig. 4. Lastly, we apply a cut on the parent rapidity to ensure a more uniform acceptance for the decay daughters.

The charged kaon decay reconstruction method is based on the fact that the four dominant $K^\pm$ decay channels [shown in relation (7)] have the same pattern. The charged kaon decays into one or two neutral daughters which are not detected and one charged daughter which is observed in the TPC.

$$K^\pm \rightarrow \begin{cases} \mu^\pm + \nu_\mu & (63.4\%), \\ \pi^\pm + \pi^0 & (21.1\%), \\ \mu^\pm + \pi^0 + \nu_\mu & (3.27\%), \\ \pi^\pm + \pi^0 + \pi^0 & (1.73\%). \end{cases} \tag{7}$$

The decay topology corresponding to the above channels is known as a "kink," as the track of the charged parent in the TPC appears to have a discontinuity at the point of the parent decay. The kink finding software starts by looping over all tracks reconstructed in the TPC in the given event, looking for pairs of tracks which are compatible with the kink pattern described

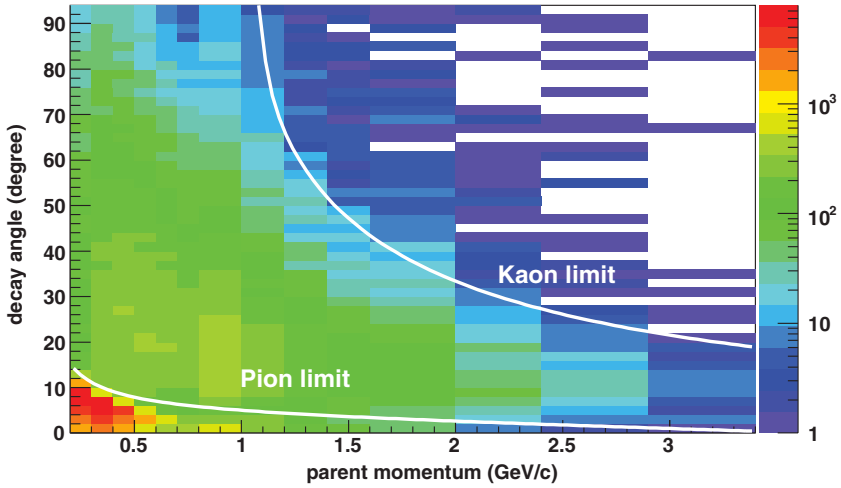

FIG. 5. (Color online) Kink angle cut regions for K^+ and K^- identified via the kink method. Particles falling between the two lines are selected.

above. The first selection criterion is for the kaon decay vertex (the kink) to be found in a fiducial volume in the TPC. The TPC has an inner radius of 50 cm and an outer radius of 200 cm from the nominal beamline, but the fiducial volume is defined to have an inner radius of 133 cm and an outer radius of 179 cm. The fiducial volume is chosen to suppress background due to high track densities (inner cut) while allowing a reasonable track length for the determination of the daughter momentum (outer cut). This leads to a maximum number of hits for both the parent and daughter track in the fiducial volume. Additional cuts are applied to the found track pairs in order to select the kink candidates.

For each kink found, a mass hypothesis is given to both the parent and daughter tracks (i.e., K^+ parent and μ^+ daughter), and the pair invariant mass is calculated based on this hypothesis. A cut on the invariant mass (m_{inv} in Table III) can then be applied. As charged pions decay with a branching ratio of approximately 100% into the same $\mu + \nu_\mu$ channel as the charged kaons, they will have the same track decay topology in the TPC. We therefore expect that the kink finding algorithm described above will include K^+, K^-, π^+, and π^- as kink parent candidates. Therefore, several other cuts must be applied to further eliminate the pion background from the kaon decays in which we are interested. A summary of the applied cuts is given in Table III.

TABLE III. Summary of cuts used in the kink analysis. The notation is as follows: $p \equiv$ parent particle momentum, $M1 \equiv (m_\pi^2 - m_\mu^2)/2m_\mu$, and $M2 \equiv (m_K^2 - m_\mu^2)/2m_\mu$. Candidates that do not satisfy the tabulated requirements are removed from the data sample. See text and Fig. 5 for further details.

Cut	$K^\pm$ (kinks)
Invariant mass	$0.3 < m_{\text{inv}} < 1.0$ GeV/c^2
Kink angle	$\begin{cases} > \text{asin}\,(M1/p) + 4.0 - 1.25 \times p & M1/p < 1, \\ < \text{asin}\,(M2/p) \quad \text{if} \quad & M2/p < 1. \end{cases}$
Daughter mom.	>100 MeV/c
DCA/cm between parent-daughter	$< 0.123 + 0.082/[p_T/(\text{GeV}/c)]^{1.153}$

In Fig. 5 we show the regions excluded by the kink angle cut in Table III. Particles falling in the region between the two lines, which are given by the relations in the "Kink angle" row of Table III, are selected. The second and third factors in the lower limit of the kink angle ($4.0 - 1.25 \times p$ in Table III) were determined using simulations to account for resolution effects. The parent-daughter DCA cut in the last row of Table III was determined from a two-dimensional (DCA and p_T) study of the background. The appropriate cut level was determined in each (DCA, p_T) cell and the results were fit with a function of the form $A + (Bp_T^{-C})$. The resulting parameters A, B, and C are given in Table III. In addition to the cuts listed in Table III, a cut was applied to the parent track dE/dx to remove pion contamination below $p_T = 500$ MeV/c, where the kaon and pion dE/dx bands are clearly separated.

C. Signal extraction

To extract the particle yield and $\langle p_T \rangle$, we build invariant mass distributions in several p_T bins for each of the particle species except the charged kaons. The residual background in each p_T bin is then subtracted through a method referred to here as "bin counting."

In the bin-counting method, three regions are defined in the invariant-mass distribution. The first, which is defined using the Gaussian signal width found by fitting the p_T-integrated invariant-mass distribution with a linear function plus a Gaussian, is the region directly under the mass peak ($\pm 3.5\sigma$, $\pm 4.5\sigma$, and $\pm 2.5\sigma$ for the K^0_S, Λ, and Ξ, respectively) which includes both signal and background (red or lightly shaded in Fig. 4). For the K^0_S and Λ invariant mass distributions, the second and third regions (blue or dark shading in Fig. 4) are defined to be the same total width as the signal region placed on either side (1σ away for K^0_S and Λ) of the chosen signal region. For the Ξ, the second and third regions are each the size of the signal region and are placed 4σ away. In p_T bins where the background appears to deviate significantly from the linear approximation, a second degree polynomial fit is used to determine the background under the mass peak. This occurs mainly at low p_T.

This procedure is carried out in each transverse momentum bin and as a function of event multiplicity. The resulting spectrum is then corrected for vertex finding efficiency (Sec. III A) as well as the particle specific efficiency and acceptance (Sec. III D). The Λ and $\overline{\Lambda}$ spectra are further corrected for higher-mass feed down as detailed in Sec. III E.

D. Particle reconstruction efficiencies

The number of reconstructed strange particles is less than the actual number produced in the collision because of the finite geometrical acceptance of the detector and the efficiency of the tracking and decay finding software. Additionally, the quality cuts described in Sec. III B reduce not only the combinatorial background but also the raw signal.

To determine the efficiency for each particle species as a function of transverse momentum, an embedding process, similar to that described in Sec. III A, is employed. In this process, a Monte Carlo generator is used to produce the particles of interest with a given transverse momentum distribution. The produced particles are propagated through the GEANT detector simulation, and the resulting signals are embedded into real events at the level of the detector response (pixel level). Using real events provides a realistic tracking and finding environment for evaluating the performance of the software. Only one simulated particle is embedded in any given event so as not to overly modify the tracking and finding environment. The embedded events are then processed with the full reconstruction software chain, and the results compared with the input to determine the final correction factors for the transverse momentum spectra. Whether or not the event used for embedding already contained one or more strange particles is not a concern as only GEANT-tagged tracks are counted for the purpose of calculating efficiencies. The resulting total efficiencies (acceptance $\times$ tracking, finding, and cut efficiencies) are plotted in Fig. 6 for K^0_S, $K^{\pm}$, Λ, Ξ, and Ω. The correction is assumed to be constant over the measured rapidity region.

Finally, a correction needs to be applied to the raw particle yields due to low primary vertex efficiencies for low multiplicity events described in Sec. III A. The spectra were binned in multiplicity classes, and for each class the particle yields were corrected using the probabilities corresponding to finding a good vertex in an event with at least a V0 candidate (open squares in Fig. 3), thereby accounting for particles from lost and fake events. The overall event normalization is also corrected, using the numbers corresponding to the probability of finding a vertex (black filled circles in Fig. 3), to account for the number of lost events.

E. Feed-down corrections

Ξ and Ω baryons produce a Λ as one of their decay products. The neutral Ξ ($\overline{\Xi}$) has not been measured by our experiment; therefore, for the purposes of determining the feed-down correction, the Ξ^0 ($\overline{\Xi}^0$) yield is taken to be equal to the measured Ξ^- ($\overline{\Xi}^+$) yield. In some cases, the daughter Λ can be detected as if it were a primary Λ particle. The result is a modification of the measured primary Λ p_T spectrum and an overestimation of the primary Λ yield. The amount of contamination is unique to the cuts used to find the Λ.

To correct this, Monte Carlo Ξ simulations were performed and tuned to match the measured shape and yield of the Ξ p_T spectrum presented in this paper. Using these simulations, the finding efficiency for secondary Λ particles was determined to be the same whether the Λ comes from a charged or a neutral Ξ. Therefore, the final feed-down correction is doubled to account for feed down from Ξ^0 decays. The shape and yield of the Λ spectrum coming from Ξ decays can then be determined. The total correction factor (efficiency $\times$ acceptance) was then calculated for both primary Λ baryons and secondary Λ baryons produced by embedded Ξ^- decays (see Fig. 7). The correction factor is different for Λ baryons coming from Ξ decays. Lastly, the secondary Λ spectrum is multiplied by the correction factor for secondary Λ baryons, divided by the primary Λ correction factor, and the result is subtracted from the measured Λ spectrum. The application of the correction factor is formalized in Eq. (8),

$$\Lambda_{\mathrm{FD}}(p_T) = \Lambda_{\mathrm{Corrected}}(p_T) - \sum_i \Xi_{\mathrm{MC}}(p_T)_i R_{\mathrm{eff}}(p_T), \quad (8)$$

where $\Lambda_{\mathrm{FD}}(p_T)$ is the final feed-down corrected p_T spectrum, $\Lambda_{\mathrm{Corrected}}(p_T)$ is the non-feed-down corrected p_T spectrum (corrected for efficiency and acceptance), $\Xi_{\mathrm{MC}}(p_T)_i$ is the

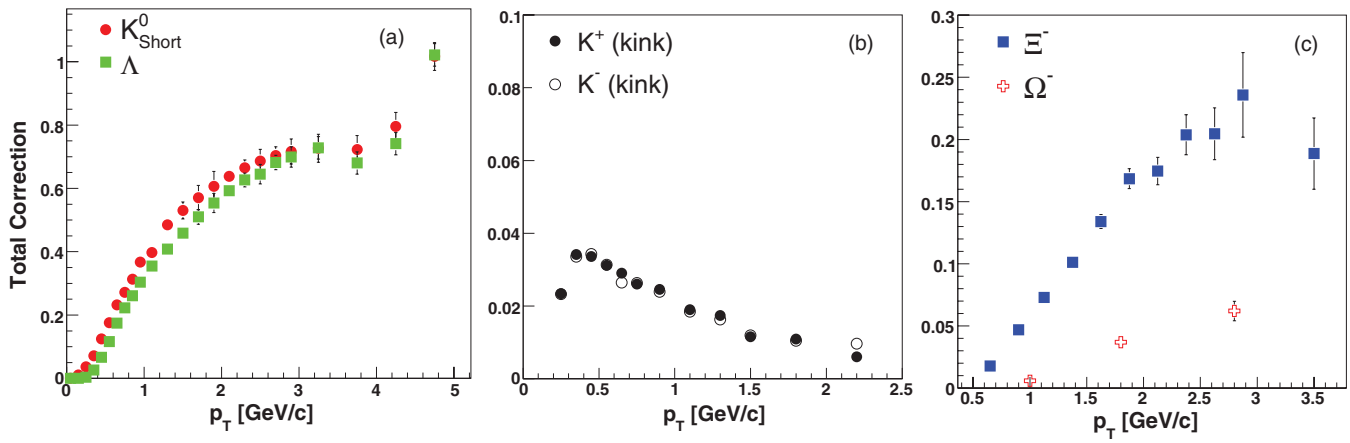

FIG. 6. (Color online) Total correction factors (efficiency $\times$ acceptance) after cuts.

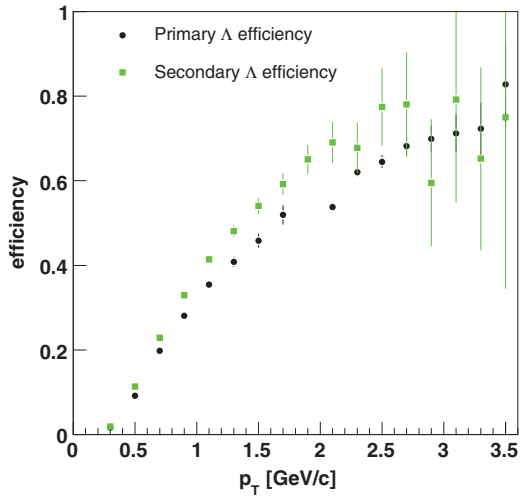

FIG. 7. (Color online) Efficiency times acceptance for primary Λ and secondary Λ from Ξ decays.

secondary p_T spectrum (determined from MC), and $R_{\text{eff}}(p_T)$ is the ratio of the secondary efficiency and acceptance correction to the primary efficiency and acceptance correction. The index i runs over the two charge states. A similar equation applies to the antiparticle states. The Ω contribution is considered negligible.

F. Systematic errors

Several sources of systematic errors were identified in the analyses. A summary of these errors and their estimated size is in Table IV. A description of various sources of systematic error and their relative contribution is given below.

1. Cuts and corrections

The offline cuts that are applied to minimize the residual backgrounds also help eliminate contamination from pileup events. The cuts may be tightened to further reduce background or loosened to allow more signal and improved statistics at the cost of greater contamination. The final cuts are a compromise between these two extremes which aim to maximize the statistics for a given particle species while eliminating as much background as possible. The systematic errors from the cut-tuning provide an estimate for our sensitivity to changes in the various cuts.

This number includes the systematic errors from the embedding and vertex finding efficiency corrections. The Λ and $\overline{\Lambda}$ entry also accounts for the systematic errors from the feed-down correction.

2. Methods of yield extraction

To estimate the systematic error on the yield extraction in each p_T bin, a second method of determining the yield in a given bin was used. In the second method, a combination of Gaussian plus a polynomial function is fit to the mass peak and background. The yield is then determined by subtracting the integral of the fitted function across the width of the signal peak from the sum of the bin content in the peak. In both methods, fitting and bin counting, a second degree polynomial fit is used in p_T bins where the background is seen to be nonlinear (at low p_T). The two methods of extracting the yield may give different values because of the finite precision of the fitting method and fluctuations in the background in the bin-counting method. The difference in the two methods and any differences resulting from a deviation from the linear background assumption are taken into account by this systematic error.

The systematic error on the midrapidity yield and $\langle p_T \rangle$ is determined using the different parametrizations of the spectra given by Eqs. (9), (10), and (11) in Sec. IV A. The error is taken to be the difference between the two parametrizations with the lowest χ^2/ndf. The final numbers for the midrapidity yield and $\langle p_T \rangle$ (in Tables VI and VII) for each particle were taken from the fit with the smallest χ^2/ndf as shown in Table V.

3. Normalization

The overall systematic error from the vertex and trigger efficiency affects only the particle yields and does not change the shape of the spectra. However, the vertex finding efficiency depends on the beam luminosity. The number quoted in this

TABLE IV. Summary of systematic errors from various sources. Errors from yield extraction and fit function for Ξ are from comparison between m_T-exponential and power-law fits. The normalization error affects only the particle yields.

Error source	K^0_S		$K^{\pm}$ (kinks)		$\Lambda(\overline{\Lambda})$		$\Xi(\overline{\Xi})$		$\Omega + \overline{\Omega}$	
	dN/dy	$\langle p_T \rangle$	dN/dy	$\langle p_T \rangle$	dN/dy	$\langle p_T \rangle$	dN/dy	$\langle p_T \rangle$	dN/dy	$\langle p_T \rangle$
Cuts and corrections (%)	5.4	1.1	3.7	2.2	5.4	1.3	13	1.1	15	8.0
Yield extraction and fit function (%)	4.9	3.7	1.5	1.2	6.3	4.7	30	5.6	20[a]	3.0[a]
Normalization (%)	4	N/A	4	N/A	4	N/A	4	N/A	4	N/A
Total (%)	8.3	3.9	5.6	2.5	9.2	4.9	33	5.7	25[a]	8.5[a]

[a]For yield extraction only; statistics do not allow a meaningful fit function study for $\Omega + \overline{\Omega}$.

TABLE V. Summary of χ^2 per degree of freedom values for different fit functions to the p_T spectra. $\Omega^- + \overline{\Omega}^+$ statistics are considered insufficient for a fit comparison.

Particle	m_T exponential		Power law		Lévy	
	χ^2/ndf	ndf	χ^2/ndf	ndf	χ^2/ndf	ndf height
K^0_S	15	22	1.5	21	0.89	19
K^+ (kinks)	3.1	11	7.0	10	0.40	9
K^- (kinks)	9.4	11	5.0	10	0.30	9
Λ	4.5	22	3.3	21	0.81	18
$\overline{\Lambda}$	4.7	22	3.1	21	0.99	18
Ξ^-	0.84	9	1.4	8	0.76	8
$\overline{\Xi}^+$	1.4	9	0.96	8	0.83	8
$\Omega^- + \overline{\Omega}^+$	0.13	1			–	

row is the level of fluctuation in the vertex finding efficiency with beam luminosity, 4%.

Conversion of our measurements to cross sections must also account for an additional 7.3% uncertainty in the measured NSD trigger cross section (26±1.9 mb) and for the 86% efficiency of the BBC trigger detectors.

IV. RESULTS

A. Spectra

The fully corrected p_T spectra for K^+, K^-, K^0_S, Λ, Ξ, and Ω are shown in Fig. 8. The measured spectra cover only a limited range in transverse momentum, and therefore an appropriately parametrized function is needed to extrapolate into the unmeasured p_T regions for the yield determination. In the past, exponential functions such as that given in Eq. (9) have been used to extrapolate spectra from $p + p$ collisions to low transverse momentum, while QCD-inspired power-law functions [see Eq. (10)] seem to provide a better description of the high p_T ($\gtrsim 3$ GeV/c) region [1,14–17]. The p_T coverage of the STAR detector for strange particles is large enough that a function which accounts for both the power-law component of the spectra and the low p_T turnover becomes necessary to

TABLE VI. Summary of midrapidity NSD yields for measured strange particles. Numbers in rows marked (FD) have been corrected for feed down as described in Sec. III E.

Particle	dN/dy, $\lvert y\rvert < 0.5$	Stat. err.	Sys. err.
K^0_S	0.134	0.003	0.011
K^+ (kinks)	0.140	0.006	0.008
K^- (kinks)	0.137	0.006	0.007
Λ	0.0436	0.0008	0.0040
$\overline{\Lambda}$	0.0398	0.0008	0.0037
Λ (FD)	0.0385	0.0007	0.0035
$\overline{\Lambda}$ (FD)	0.0351	0.0007	0.0032
Ξ^-	0.0026	0.0002	0.0009
$\overline{\Xi}^+$	0.0029	0.0003	0.0010
$\Omega^- + \overline{\Omega}^+$	0.00034	0.00016	0.0001

TABLE VII. A summary of midrapidity $\langle p_T \rangle$ for measured strange particles. Feed-down corrected numbers for Λ and $\overline{\Lambda}$ are the same as the non-feed-down corrected values within statistical errors.

Particle	$\langle p_T \rangle$ (GeV/c)	Stat. err.	Sys. err.
K^0_S	0.605	0.010	0.023
K^+ (kinks)	0.592	0.071	0.014
K^- (kinks)	0.605	0.072	0.014
Λ	0.775	0.014	0.038
$\overline{\Lambda}$	0.763	0.014	0.037
Λ (FD)	0.762	0.013	0.037
$\overline{\Lambda}$ (FD)	0.750	0.013	0.037
Ξ^-	0.924	0.120	0.053
$\overline{\Xi}^+$	0.881	0.120	0.050
$\Omega^- + \overline{\Omega}^+$	1.08	0.29	0.09

describe the data. A form that has been suggested is the Lévy function given by Eq. (11) [18],

$$\frac{1}{2\pi p_T}\frac{d^2N}{dy\,dp_T} = Ae^{\frac{-m_T}{T}}, \tag{9}$$

$$\frac{1}{2\pi p_T}\frac{d^2N}{dydp_T} = B\left(1+\frac{p_T}{p_0}\right)^{-n}, \tag{10}$$

$$\frac{1}{2\pi p_T}\frac{d^2N}{dydp_T} = \frac{dN}{dy}\frac{(n-1)(n-2)}{2\pi nC[nC+m_0(n-2)]} \times\left(1+\frac{\sqrt{p_T^2+m_0^2}-m_0}{nC}\right)^{-n}, \tag{11}$$

where $A, T, B, p_0, n, \frac{dN}{dy}, C$, and m_0 are fit parameters. Attempts were made to fit the p_T spectra for our measured species with all three forms. A summary of the resulting χ^2/ndf from each fit is given in Table V for each of the measured species. The midrapidity yields and mean transverse momenta quoted below were determined from the best fitting form which, for all species except the low statistics Ω, was the Lévy form [Eq. (11)]. An m_T exponential was used to determine the Ω yield and $\langle p_T \rangle$. The measured midrapidity yields and feed-down corrected yields are presented in Table VI. The measured mean transverse momenta are presented in Table VII.

Initially, we compare our measurement of neutral strange particles to similar experiments at this energy. The closest comparison can be made to the S$p\bar{p}$S (Super Proton-Antiproton Synchrotron) experiments of UA1-UA5 using the $p + \bar{p}$ beam. Only UA5 published strange particle measurements at $\sqrt{s} = 200$ GeV [14,15], with others at $\sqrt{s} = 546$ [19] and 900 GeV [14,15], while UA1 published high statistics strange particle measurements at $\sqrt{s} = 630$ GeV ([1] and references cited therein).

It is worth noting that the UA5 Λ sample consisted of only 168 "manually sorted" candidates [14], whereas the STAR sample consists of 58000 candidates.

Table VIII compares the values of dN/dy and those obtained from the STAR p_T spectra to the published values

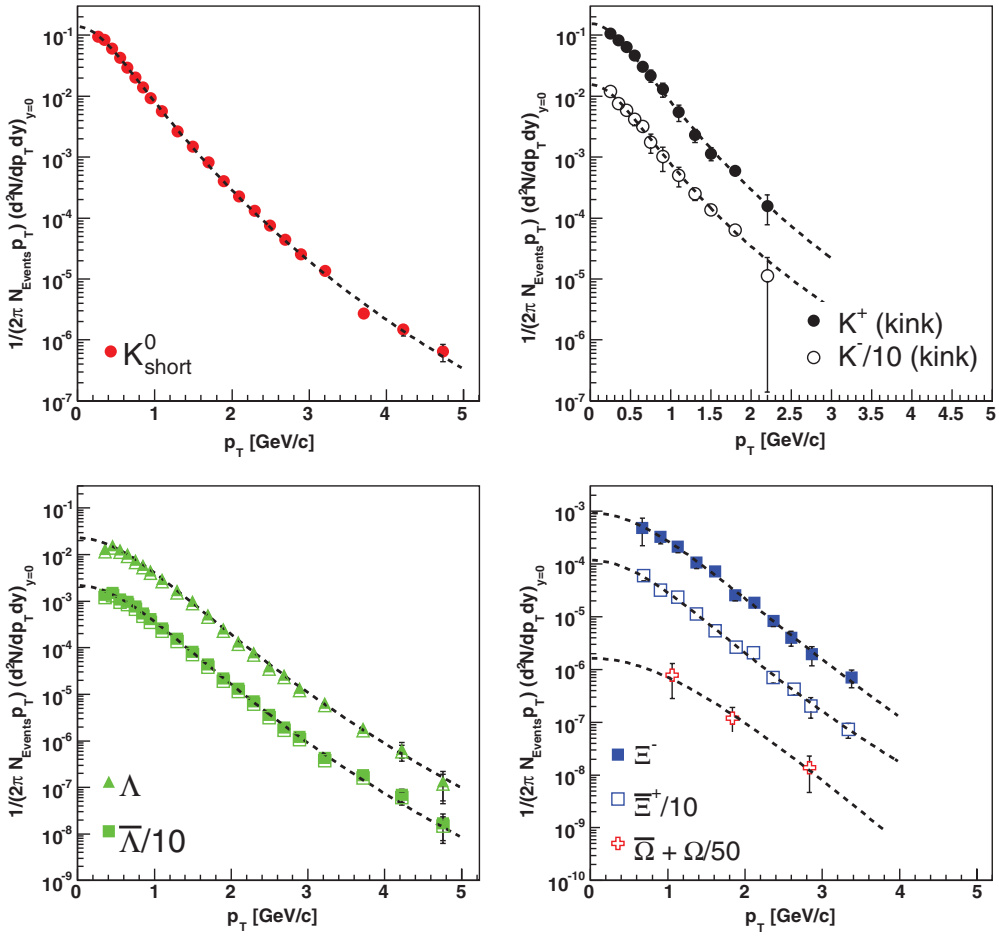

FIG. 8. (Color online) Corrected midrapidity ($|y| < 0.5$) p_T spectra for K^+, K^-, K^0_S, Λ, Ξ, and Ω. Λ spectra corrected for feed-down are shown as open symbols in the Λ panel. Dashed lines are fits using Eq. (11) except for the $\Omega + \overline{\Omega}$ where the fit uses Eq. (9). Error bars include systematic errors, while the fits were done using only statistical errors for all species except the charged kaons.

from the UA5 experiment at $S p\bar{p}S$ [15] measured with a larger rapidity interval. In the last column, the STAR data are scaled by a factor, obtained via PYTHIA [20] simulation, to account for the difference in rapidity coverage of the two experiments. UA5 measured K^0_S with $|y| < 2.5$, Λ with $|y| < 2.0$, and Ξ with $|y| < 3.0$. STAR measures only in the region $|y| < 0.5$. The STAR scaled yields are found to agree with the measurement from UA5 and have greatly improved on the precision.

TABLE VIII. Comparison of yields from UA5 (K^0_S from Ref. [15], Λ from Ref. [14]) and NSD yields from STAR. STAR entries in the last column have been scaled to the UA5 acceptance using PYTHIA [20]. STAR errors include systematics. UA5 errors include their estimated 20% systematic error.

Particle	STAR dN/dy ($\|y\| < 0.5$)	UA5 yield	STAR yield (scaled to UA5 y)
K^0_S	0.134 ± 0.011	0.73 ± 0.18, $\|y\| < 3.5$	0.626 ± 0.051
$\Lambda + \overline{\Lambda}$	0.0834 ± 0.0056	N/A	0.272 ± 0.018
$\Lambda + \overline{\Lambda}$ (FD)	0.0736 ± 0.0048	0.27 ± 0.09, $\|y\| < 2.0$	0.240 ± 0.016
$\Xi + \overline{\Xi}$	0.0055 ± 0.0014	$0.03^{+0.04}_{-0.02}$, $\|y\| < 3.0$	0.0223 ± 0.0057

Table IX compares the $\langle p_T \rangle$ of the two experiments. It was verified, using PYTHIA, that the dependence of $\langle p_T \rangle$ on the different rapidity intervals between STAR and UA5 is small, i.e., 2–3%. Therefore, the STAR $\langle p_T \rangle$ measurement is compared to UA5 without further scaling and is found to have improved on the precision.

TABLE IX. Comparison of $\langle p_T \rangle$ (GeV/c) from UA5 and STAR. STAR errors include systematics; UA5 errors include their estimated 20% systematic error.

Particle	STAR $\langle p_T \rangle (\|y\| < 0.5)$	UA5 $\Lambda \langle p_T \rangle$
K^0_S	0.61 ± 0.02	$0.53^{+0.13}_{-0.12}$, $\|y\| < 2.5$
$\Lambda + \overline{\Lambda}$	0.77 ± 0.04	$0.8^{+0.26}_{-0.21}$, $\|y\| < 2.0$
$\Xi + \overline{\Xi}$	0.903 ± 0.13	$0.8^{+0.4}_{-0.2}$, $\|y\| < 3.0$

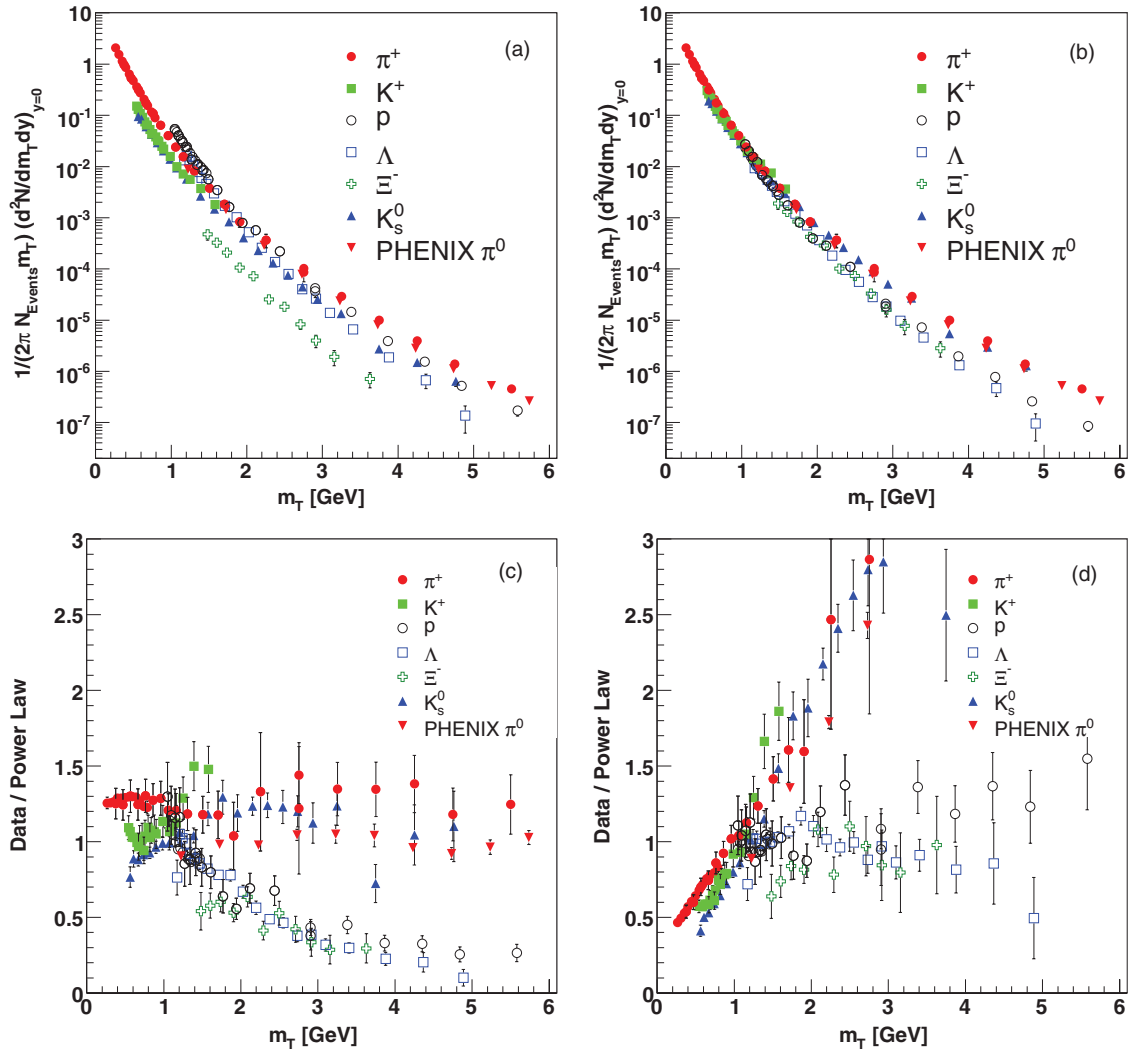

FIG. 9. (Color online) Comparison of (a) unscaled and (b) scaled transverse mass midrapidity ($|y| < 0.5$) spectra for π, K^+, K^0_S, p, Λ, and Ξ from $p + p$ collisions in STAR and PHENIX studies at $\sqrt{s} = 200$ GeV. STAR π, K, and p spectra are from Refs. [26–28]; PHENIX π^0 spectrum is from Ref. [17]. Ratios of data to power-law fits for each data point in (b) are given in (c) for meson fits and (d) for baryon fits. Error bars include systematics.

B. Transverse mass scaling

Previous work noted that the identified particle spectra from $p + p$ collisions at ISR energies [21,22] seem to sample an approximately universal curve when plotted against transverse mass [23], an effect termed "m_T scaling." More recently, data from heavy ion collisions at RHIC have been shown to scale in transverse mass over the measured range available [24]. Transverse mass spectra from identified hadrons at $\sqrt{s} =$ 540 GeV and 630 GeV $p + \overline{p}$ collisions at S$p\bar{p}$S have also been shown to exhibit the same behavior up to at least 2.5 GeV [24]. The degree to which m_T scaling is applicable and the resulting scaling factors have been used to argue for the presence of a gluon-saturated state (color-glass condensate) in heavy ion collisions at RHIC energies [25], though no such interpretation is applied to $p + p$ or $p + \overline{p}$ collisions. Little discussion of the similarity of the results between $p + p$ and $A + A$ has been provided. In Fig. 9(a), we present the K^0_S, Λ, and Ξ m_T spectra together with their antiparticles and with m_T spectra for π, K, and p from previously published STAR $p + p$ results at $\sqrt{s} = 200$ GeV [26–28]. The PHENIX π^0 spectrum from $p + p$ collisions at the same energy is also shown [17].

It is clear from Fig. 9(a) that while the spectra appear to have qualitatively similar shapes, the yields are quite different. Nevertheless, the shape similarities encourage us to find a set of scaling factors that would bring the spectra onto a single curve. Figure 9(b) shows the result of scaling with the set of factors shown in Table X. These factors were chosen so as to match the π, K, and p spectra at an m_T of 1 GeV. The higher mass spectra are then scaled to match the π, K, and p spectra in their respective regions of overlap.

While the low-m_T region seems to show reasonable agreement between all the measured species, the region above $m_T \sim 2$ GeV shows an interesting new effect. The meson spectra appear to be harder than the baryon spectra with as much as an order of magnitude difference developing by

TABLE X. Summary of scaling factors applied to the transverse mass spectra in Fig. 9(b). Second row lists the transverse mass (in GeV) at which a given particle is scaled to match the other spectra.

	π	K	p	Λ	Ξ
Scaling factor	1.0	2.0	0.6[a]	0.7	4.0
Scaled at m_T	1.0	1.0	1.0	1.5	1.5

[a]Data from Ref. [26] were scaled by 0.45.

4.5 GeV in m_T. To quantify the meson-baryon difference in spectral shape, two power-law fits were made, one to all the scaled meson m_T spectra and another to the baryon m_T spectra. The ratio of data to the corresponding fit was taken for each point in Fig. 9(b). The data-to-fit ratio is shown for the meson fit in Fig. 9(c) and the baryon fit in Fig. 9(d).

This is the first time such a meson-baryon effect has been noticed in $p + p$ collisions. This effect is observable due to the high p_T (and therefore high m_T) measurement of the strange particle spectra (this work) and spectra from the "relativistic rise" region [28]. The harder meson spectrum in the jet-like high m_T region may indicate that for a given jet energy, mesons are produced with higher transverse momentum than baryons. This effect would be a simple reflection of the fact that meson production from fragmentation requires only a (quark, antiquark) pair, while baryon production requires a (diquark, antidiquark) pair. The difference between the baryon and meson curves appears to be increasing over our measured range, and it will be interesting to see, with greater statistics, what level of separation is achieved and whether the spectra eventually become parallel.

C. Particle ratios

Figure 10(a) shows the mean antibaryon/baryon ratios ($\overline{B}/B$) as a function of strangeness content for $p + p$ and Au+Au at $\sqrt{s} = 200$ GeV [29]. The ratios rise slightly with increasing strangeness content and are consistent within errors with those from Au+Au collisions at the same center-of-mass energy. Although the $\overline{B}/B$ ratios are not unity for the protons and Λ baryons, the deviation from unity may be explained by different parton distributions for the light quarks [30]. This may be sufficient to explain the observed deviation from unity without having to invoke baryon number transport over five units of rapidity.

In the case of a quark jet, it is expected that there is a leading baryon as opposed to antibaryon while there is no such distinction for a gluon jet. Therefore, making the assumption that at high p_T the observed hadron production mechanisms are dominated by quark-jet fragmentation, it is reasonable to expect that the $\overline{B}/B$ ratio will drop with increasing p_T. This has been predicted previously for calculations starting from as low as 2 GeV/c [31]. Figures 10(b) and 10(c) show the $\overline{\Lambda}/\Lambda$ and $\overline{\Xi}/\Xi$ ratios as a function of transverse momentum, respectively. Although the errors shown in these figures are large, the ratios show no sign of decrease in the measured range. The dotted horizontal line in each figure is the error-weighted average over the measured p_T range.

One conclusion that could be drawn from the ratios in Fig. 10 is that particle production is not predominantly the result of quark-jet fragmentation over our measured range of p_T.

D. Mean transverse momentum

One means of partially characterizing the p_T spectra from $p + p$ collisions is through the determination and comparison of the mean transverse momentum. In Fig. 11, the $\langle p_T \rangle$ is shown for all particle species measured in both $p + p$ and central Au+Au collisions in STAR.

In total, 12 particles in both systems are presented, covering a mass range of approximately 1.5 GeV/c^2. The solid line is an empirical curve proposed originally [32] to describe the ISR [33] and Fermilab [34] data for only π, K, and p, at $\sqrt{s} = 25$ GeV. It is interesting that it fits the STAR lower mass particles from $p + p$ at $\sqrt{s} = 200$ GeV remarkably well considering there is nearly an order of magnitude difference

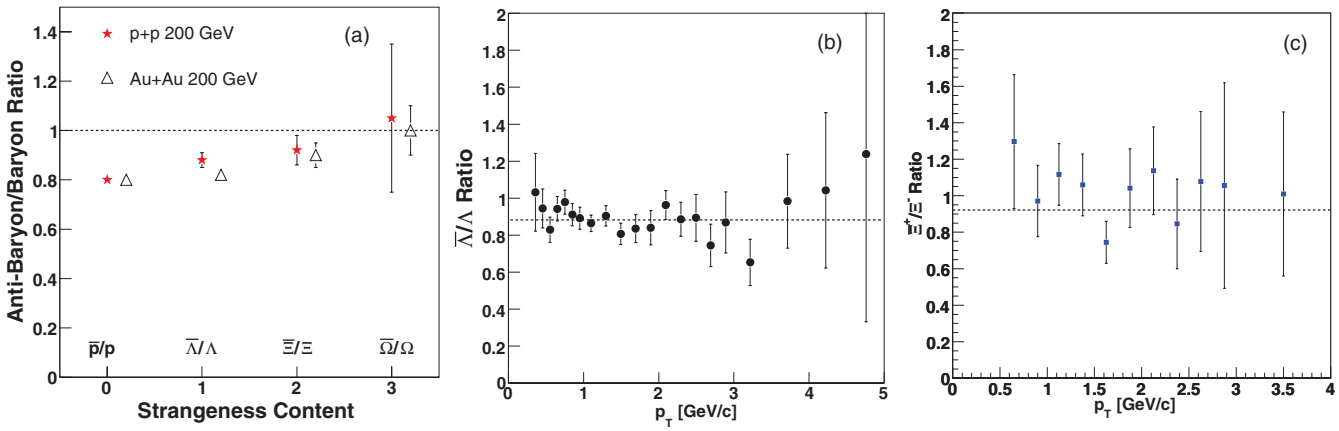

FIG. 10. (Color online) Panel (a) shows the p_T averaged ratios vs strangeness content for our measured species compared with measurements from Au+Au; dashed line is at unity for reference. Panels (b) and (c) show midrapidity ($|y| < 0.5$) ratios of $\overline{\Lambda}$ to Λ and $\overline{\Xi}^+$ to Ξ^- vs p_T; dashed lines in (b) and (c) are the error-weighted means over the measured p_T range, 0.882 ± 0.017 for $\overline{\Lambda}/\Lambda$, 0.921 ± 0.062 for $\overline{\Xi}/\Xi$. Error bars are statistical only.

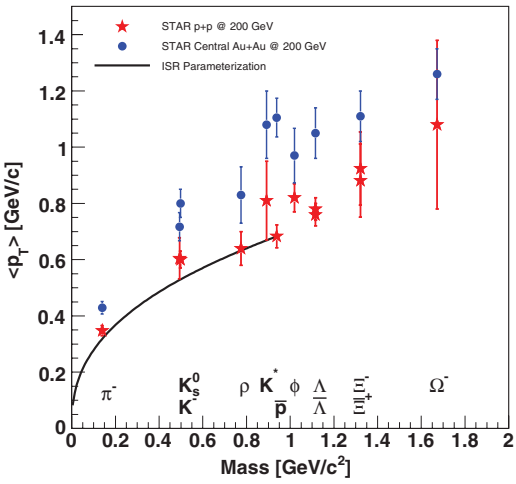

FIG. 11. (Color online) $\langle p_T \rangle$ vs particle mass for different particles measured by STAR. Error bars include systematic errors. The ISR parametrization is given in Ref. [32].

in collision energy. The dependence of the inverse slope parameter T (and therefore of the $\langle p_T \rangle$) on particle mass has previously been proposed to be due to an increasing contribution to the transverse momentum spectra from minijet production in $p + p$ and $p + \overline{p}$ collisions [35]. The contribution is expected to be even greater for higher mass particles [36].

The available statistics allow a detailed study to be made. The midrapidity p_T spectra can be binned according to eventwise charged particle multiplicity (uncorrected $dN_{\rm ch}/d\eta$) and the $\langle p_T \rangle$ determined in each bin. We present in Fig. 12 the dependence of $\langle p_T \rangle$ on uncorrected charged particle multiplicity for K^+, K^-, K^0_S, Λ, and Ξ.

The scale difference is readily apparent; but perhaps more interesting is the increasing trend of $\langle p_T \rangle$ with event multiplicity. The increase in $\langle p_T \rangle$ with multiplicity is slightly faster for the Λ than for the K^0_S and charged kaons over the

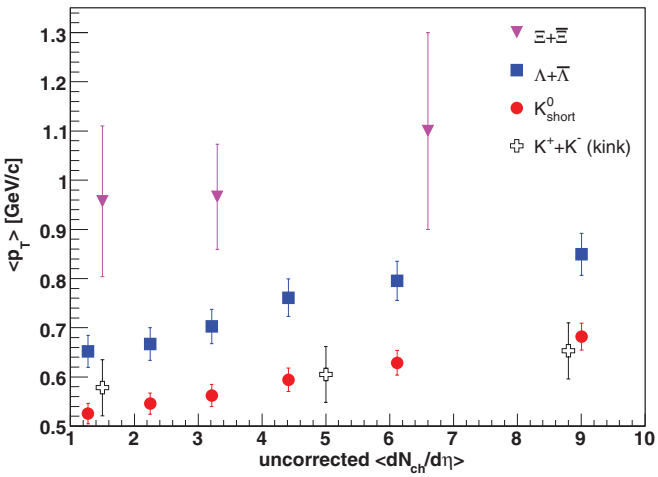

FIG. 12. (Color online) $\langle p_T \rangle$ vs charged multiplicity for K^+, K^-, K^0_S, $\Lambda + \overline{\Lambda}$, and $\Xi + \overline{\Xi}$. The points for $\Xi + \overline{\Xi}$ have been determined using only the measured region. Error bars are statistical only. See text for more details.

range from 2 to 6 in $\langle dN_{\rm ch}/d\eta \rangle$. The statistics available in the multiplicity-binned $\Xi + \overline{\Xi}$ do not allow a proper constraint of the Lévy fit. The points for $\Xi + \overline{\Xi}$ shown in Fig. 12 were determined from the error-weighted mean of the measured p_T distribution only. The present level of error on the Ξ measurement does not allow a strong conclusion to be drawn. A mass ordering of the $\langle p_T \rangle$ multiplicity dependence has been observed in previous measurements at three different energies [3] and has been explained as being due to a stronger correlation for heavy particles with minijets [5]. In particular, the pions show little increase in $\langle p_T \rangle$ when going from low to high multiplicity collisions [3].

Models inspired by pQCD such as PYTHIA suggest that the number of produced minijets (and thereby the event multiplicity) is correlated with the hardness Q^2 of the collision. The effect of the minijets is to increase the multiplicity of the events, and their fragmentation into hadrons will also produce harder p_T spectra.

The spectral shape cannot be characterized by a single number. It is also possible to compare the multiplicity-binned spectra directly. We show in Figs. 13(a) and 13(b) the ratio R_{pp} of the multiplicity-binned p_T spectra to the multiplicity-integrated (minimum bias) spectra scaled by the mean multiplicity for each bin [see Eq. (12)] for K^0_S and Λ, respectively.

$$R_{pp}(p_T) = F_{\rm scale} \frac{dN/dp_T(\text{mult}, p_T)}{dN/dp_T(\text{minbias}, p_T)}, \tag{12}$$

where

$$F_{\rm scale} \equiv \frac{N_{\rm events}(\text{minbias})\langle N_{\rm ch}(\text{minbias})\rangle}{N_{\rm events}(\text{mult})\langle N_{\rm ch}(\text{mult})\rangle}. \tag{13}$$

The changes in incremental shape from one multiplicity bin to the next then become easier to see. The striking change in spectral shape going from the lowest to highest multiplicity bin is further evidence of the increasing contribution of hard processes (jets) to the high p_T part of the spectra in high multiplicity events.

Figure 13(c) shows the Λ/K^0_S ratio as a function of p_T in the various multiplicity bins. We see in all three bins that the Λ shows a sharper increase with p_T in the low p_T ($\lesssim 1.5$ GeV/c) part of the spectrum. Furthermore, there seems to be a relative increase in Λ production in the intermediate $1.5 \leqslant p_T \leqslant 4.0$ GeV/c region from low to high charged multiplicity.

V. MODEL COMPARISONS

A. Comparison with PYTHIA (LO pQCD)

At the present time, the most ubiquitous model available for the description of hadron+hadron collisions is the PYTHIA event generator. PYTHIA was based on the Lund string fragmentation model [37,38] but has been refined to include initial and final-state parton showers and many more hard processes. PYTHIA has been shown to be successful in the description of collisions of e^+e^-, $p + \overline{p}$, and fixed target $p + p$ systems (see, for example, Ref. [39]).

In this paper, we have used PYTHIA v6.220 (referred to hereafter as v6.2) and v6.317 (referred to as v6.3), using default

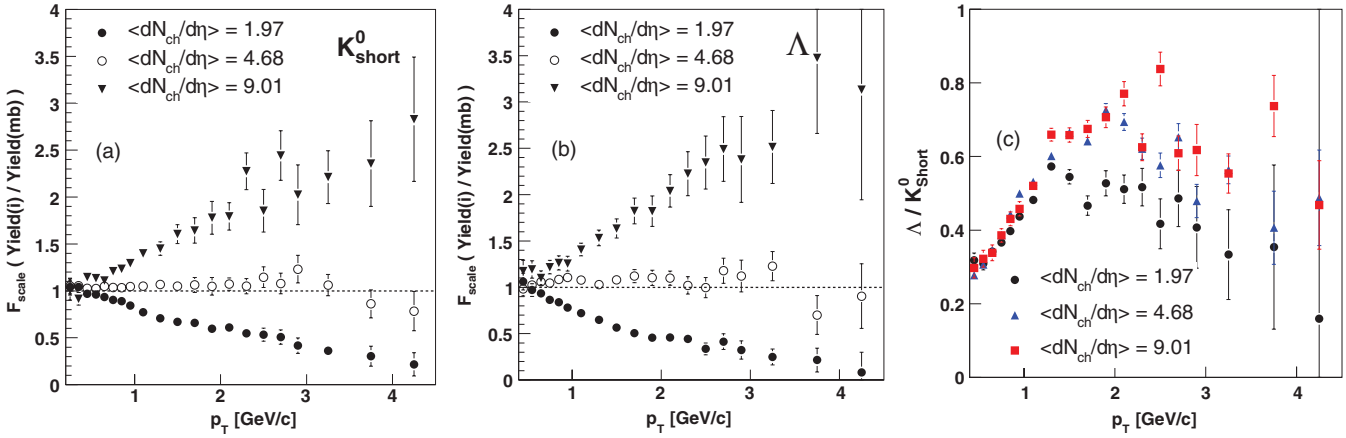

FIG. 13. (Color online) Ratios of multiplicity binned spectra to minimum bias spectra R_{pp} for (a) K^0_S and (b) Λ; and (c) ratio of the Λ spectrum to the K^0_S spectrum in each multiplicity bin. See text for further details.

settings with in-elastic cross section (MSEL = 1), in order to simulate p_T spectra for K^0_S, Λ, and Ξ. These have then been compared with the measured data.

As shown in Fig. 14, although there is some agreement at low p_T, there are notable differences above $p_T \sim 1.0$ GeV/c, where hard processes begin to dominate. PYTHIA v6.2 underestimates the Λ yield by almost an order of magnitude at $p_T = 3$ GeV/c. With the newer v6.3, released in January 2005, these large discrepancies have been largely reconciled for K^0_S but remain significant for Λ and Ξ. This version includes a significantly modified description of the multiple parton scattering processes. The dot-dashed lines in Fig. 14 represent a simple tune that was done with PYTHIA v6.3 which will be described in more detail below.

To try and understand the difference between PYTHIA and our results, we compared $\langle p_T \rangle$ against the uncorrected charged multiplicity for K^0_S and Λ, as shown in Fig. 15. As expected from the previous figure, v6.2 fails to reproduce the minimum bias magnitude of $\langle p_T \rangle$. Although v6.3 is capable of reproducing our minimum bias values of $\langle p_T \rangle$, it clearly fails to reflect its increase with charged multiplicity, suggesting that further tuning is necessary.

To improve the agreement with our data, we made some simple changes to the PYTHIA default parameters. In particular, increasing the K factor to 3 (set to 1 in the defaults) enhances the particle yield at high p_T in the model, which allows it to better describe the data.

The K factor, which represents a simple factorization of next-to-leading-order (NLO) processes in the PYTHIA leading-order (LO) calculation, is expected to be 1.5–2 for most processes, such as Drell-Yan and heavy quark production [40] at higher energies. A K factor of 3, as suggested by this measurement, would signal a large NLO contribution, particularly for light quark production at RHIC energies. Interestingly, a large K factor has been estimated for the $\sqrt{s} \sim$ 200 GeV regime at RHIC based on the energy dependence of charged hadron spectra [41]. So it seems that for light quark production at lower energies, NLO contributions are important, and a comparison of our data to detailed pQCD based NLO calculations is more appropriate.

With the addition of this K factor, we can see that the p_T spectra for Λ and Ξ in Fig. 14 agree even better with the model, with the K^0_S data falling slightly below the prediction. More importantly, the PYTHIA results of $\langle p_T \rangle$ vs charged multiplicity,

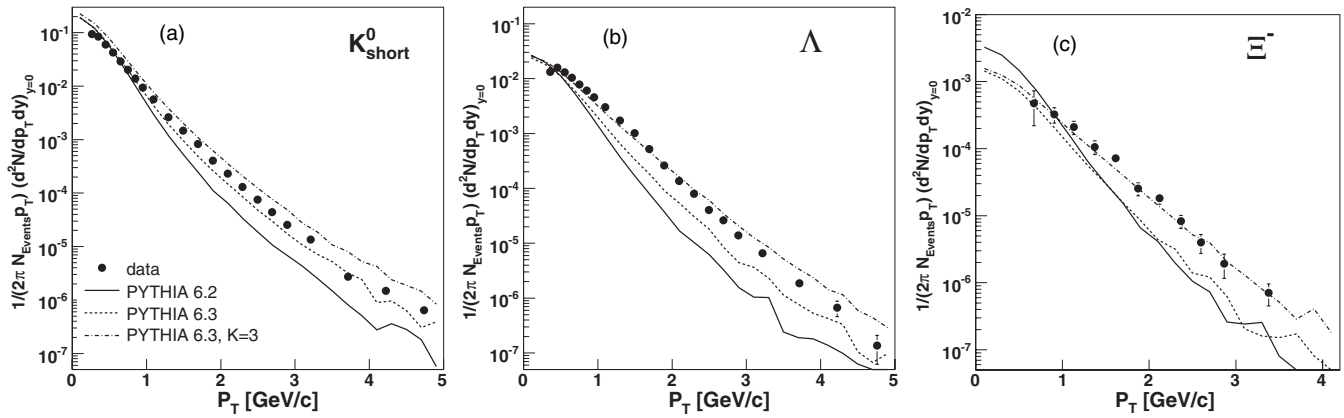

FIG. 14. (a) K^0_S , (b) Λ, and (c) Ξ^- p_T spectra compared with PYTHIA(v6.2 MSEL = 1, and v6.3) with the default K factor of 1 (solid and dashed curves, respectively), and K factor of 3 (dot-dashed curve).

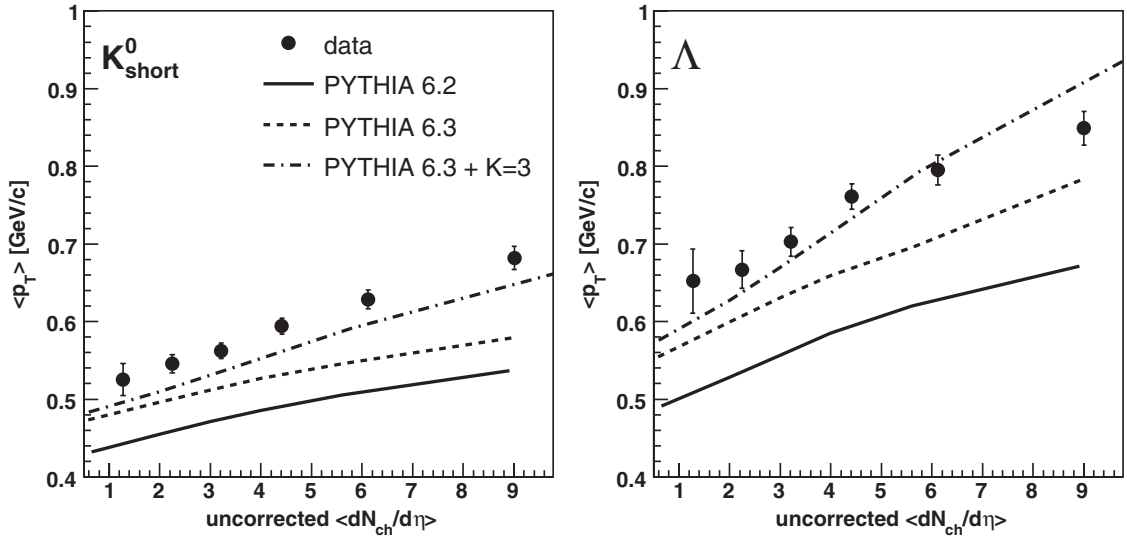

FIG. 15. K^0_S and Λ multiplicity-binned $\langle p_T \rangle$ compared to PYTHIA v6.2 default (solid curve) and v6.3 default (dashed curve) and v6.3 with K factor of 3 (dot-dashed curve).

including the enhanced K factor, are now in much better agreement with the data, as seen in Fig. 15.

Figure 16 shows the results of separating PYTHIA events based on their final state parton content. Events for which the final state is qq are labeled as containing quark jets, while events with gg are labeled as containing gluon jets. Figure 16(a) shows that events with only quark-jet final states seem to show a mass splitting in the high m_T region, while events whose final states contain gluon jets [Fig. 16(b)] show a shape difference between mesons and baryons with the meson spectra being harder than the baryon spectra. The shape difference is also apparent in Fig. 16(c) which

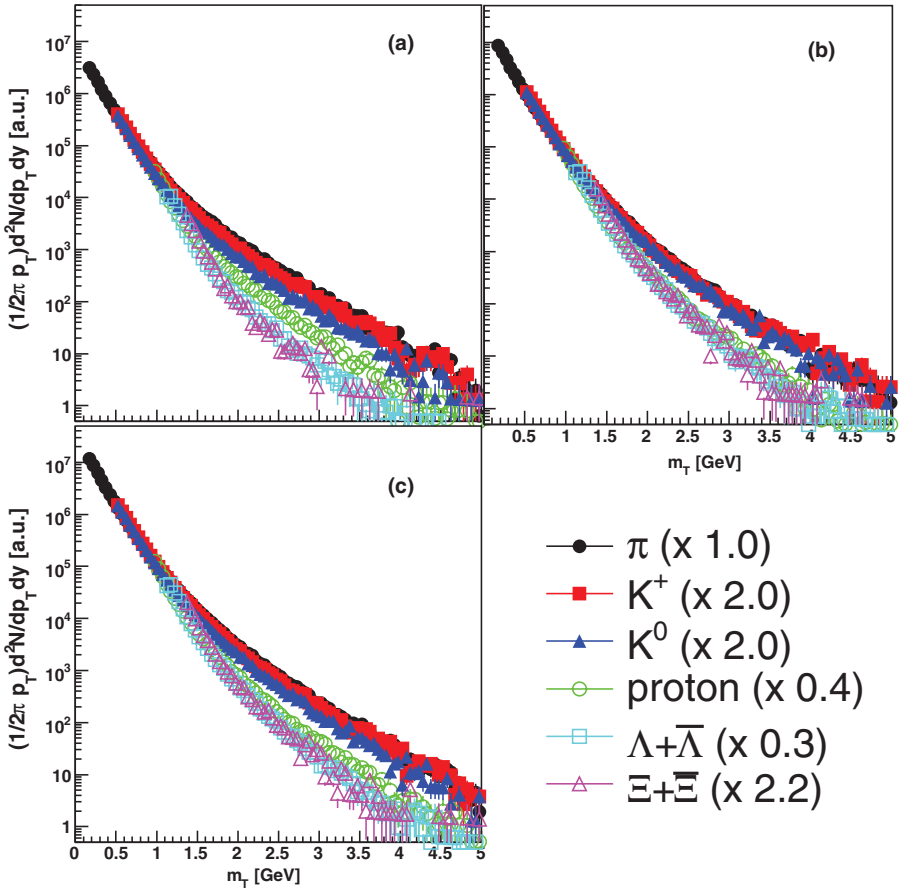

FIG. 16. (Color online) m_T scaling results from PYTHIA v6.3 with default settings. Quark- or gluon-jet selections are based on the final state partons being qq or gg, respectively. Events with (a) only quark-jet final states (qq), (b) gluon-jet (gg) and mixed final states (qg), and (c) all three final states. Spectra have been scaled by the factors listed in the legends. See text for more details.

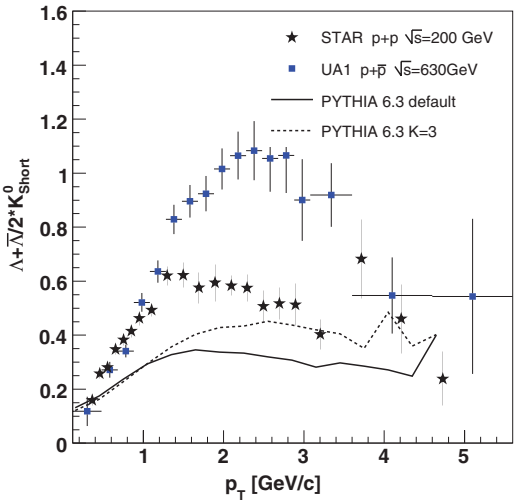

FIG. 17. (Color online) Λ/K^0_S as a function of p_T compared with PYTHIA.

contains all final states including those with both quark and gluon jets. This shape difference could be simply related to the fact that a fragmentation process could impart more momentum to a produced meson than to a produced baryon based on mass and energy arguments. This, taken together with the results shown in Secs. IV B and IV C, indicates that above 2 GeV in *transverse mass*, the spectra contain significant contributions from *gluon*-jet fragmentation rather than quark-jet fragmentation.

In Fig. 13(c), we showed the Λ to K^0_S ratio separated into multiplicity bins. Figure 17 shows the multiplicity integrated ratio compared with PYTHIA calculations using the default settings as well as a K factor of 3. Here, we see again the same shape difference between the Λ and the K^0_S that is seen for baryons and mesons in general in Fig. 9(b) and in the p/π ratio [28]. PYTHIA is not able to reproduce the full magnitude of the effect in either ratio [28]. The Λ to K^0_S ratio shows a similar shape in $\sqrt{s} = 200$ GeV Au+Au collisions, though the magnitude is larger and multiplicity dependent [42]. Also, measurements from UA1 at $\sqrt{s} = 630$ GeV indicate the magnitude may also be dependent on beam energy [1].

B. Comparison with NLO pQCD calculations

In Fig. 18 we compare the K^0_S and Λ spectra against NLO pQCD calculations including fragmentation functions for the K^0_S from Kniehl, Kramer, and Pötter (KKP) [43] and a calculation for the Λ by de Florian, Stratmann, and Vogelsang (DSV) [44]. The variations in μ show the theoretical uncertainty due to changes of the factorization and renormalization scale used. The factorization and renormalization scale allows one to weight the specific hard scattering contributions of the parton densities to the momentum spectrum. Although for the K^0_S, reasonable agreement is achieved between our data and the pQCD calculation, the comparison is much less favorable for the Λ. Considering that good agreement was achieved for charged pion [28] and π^0 [17,45] spectra and yields at the same energy, our comparison and the comparisons in Ref. [28] suggest that the region of agreement with NLO pQCD calculations may be particle species dependent. The baryons are more sensitive to the gluon and nonvalence quark fragmentation function, which is less constrained at high values of the fractional momentum z [46].

Recently, the OPAL Collaboration released new light quark flavor-tagged e^+e^- data which allow further constraint of the fragmentation functions [47]. Albino-Kniehl-Kramer (AKK) showed that these flavor-separated fragmentation functions can describe our experimental data better [48]. However, to achieve this agreement, AKK fixed the initial gluon to Λ fragmentation function (D^{Λ}_g) to that of the proton (D^p_g), and applied an additional scaling factor. They then checked that

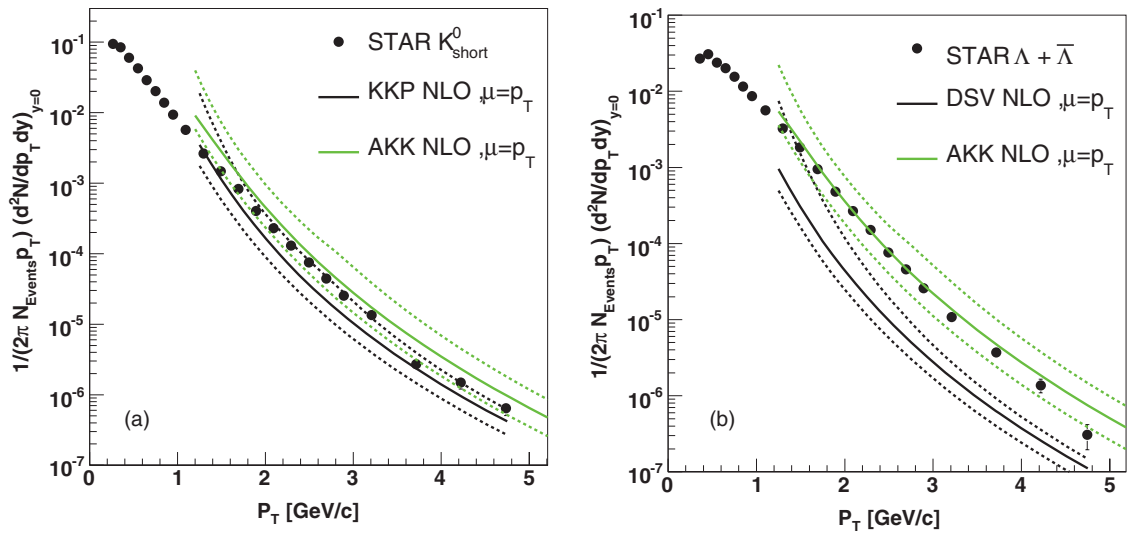

FIG. 18. (Color online) K^0_S and Λ particle spectra (circles) compared with NLO calculations by DSV and AKK based on specific (a) K^0_S [43] and (b) Λ [44] fragmentation functions. Dashed lines illustrate the uncertainty due to the choice of factorization scale μ. Upper dashed curve for each model is from $\mu = 2p_T$, solid curve from $\mu = p_T$, and lower dashed curve from $\mu = p_T/2$.

this modified D_g^{Λ} also works well in describing the $\overline{p}+p$ S$p\bar{p}$S data at $\sqrt{s}=630$ GeV. So, as can be seen from the Λ data in Fig. 18, our measurement is a good constraint for the high z part of the gluon fragmentation function. Previously obtained fragmentation functions extracted from the OPAL data (the DSV NLO calculation) do not agree well with our measurement. Similar conclusions have been drawn elsewhere with respect to the important role of RHIC energy $p+p$ collisions [49]. Recent studies of forward π^0 production also suggest that the region of agreement with NLO calculations extends as far out as 3.3 units in $\langle\eta\rangle$ [50].

C. Comparison with EPOS

In this section, we compare our data to version 1.02 of the EPOS model [51]. This model generates the majority of intermediate momentum particles by multiple parton interactions in the final state rather than hard fragmentation. The multiparton cross section is enhanced through a space-like parton cascade in the incoming parton systems. The outgoing, time-like parton emission is allowed to self-interact and to interact with the diquark remnants. The interactions can be either elastic or inelastic. The overall result is a strong probability for multiparton interactions before hadronization. The cascades are modeled through so-called parton ladders which also include multiple scattering contributions of the diquark remnants from a hard parton scattering in a $p+p$ collision. Furthermore, by taking into account the soft Pomeron interactions, the model is able to describe the $p+p$ spectra down to low p_T. Finally, the inclusion of parton ladder splitting in asymmetric $d+$Au collisions yields a good description of the difference between $p+p$ and $d+$Au spectra in the same theoretical framework. Further details of the model can be found elsewhere [51].

EPOS results shows remarkable agreement with BRAHMS, PHENIX, and STAR data for pion and kaon momentum spectra and $\langle p_T\rangle$ in $p+p$ and $d+$Au collisions at both central and forward rapidities ([28,51,52] and references therein). Figure 19 shows that this trend also continues for the heavier strange particles at midrapidity. The agreement in $p+p$ collisions in the measured p_T region is largely due to a strong soft component from string fragmentation in the parton ladder formalism. Remnant and hard fragmentation contributions are almost negligible at these moderate momenta. The soft contribution dominates the kaon spectrum out to 1 GeV/c and the Ξ spectrum out to 3 GeV/c. As the momentum differences between (diquark, antidiquark) and (quark, antiquark) string splitting are taken into account, and the current mass difference between light and strange quarks is folded into the spectral shape, a comparison between the spectra exhibits a flow-like mass dependence.

The agreement with EPOS is as good as the best NLO calculations. A detailed discussion of the differences between EPOS and NLO calculations is beyond the scope of this paper, but it should be mentioned that the two models are, in certain aspects, complementary. More measurements (a) of heavier particles and (b) to much higher p_T are needed to distinguish between the different production mechanisms. In summary, the data show the need for sizable NLO contributions or soft multiparton interactions in order to describe strange particle production in $p+p$ collisions.

D. Statistical model

The application of statistical methods to high energy hadron-hadron collisions has a long history dating back to Hagedorn in the 1960s [53–55]. Since then statistical models have enjoyed much success in fitting data from relativistic heavy ion collisions across a wide range of collision energies [56–63]. The resulting parameters are interpreted in a thermodynamic sense, allowing a "true" temperature and several chemical potentials to be ascribed to the system. More recently, statistical descriptions have been applied to $p+p$ and $\overline{p}+p$ collisions [64], and even to $e^+ + e^-$ [65]; but it remains unclear as to how such models can successfully describe particle production and kinematics in systems of small volume and energy density compared to heavy-ion collisions.

It is important to note that a $p+p$ system does not have to be *thermal* on a macroscopic scale to follow statistical emission. For example, Bourrely and Soffer have recently shown that jet fragmentation can be parametrized with statistical distributions for the fragmentation functions and parton distribution functions [46]. In this picture, the apparently

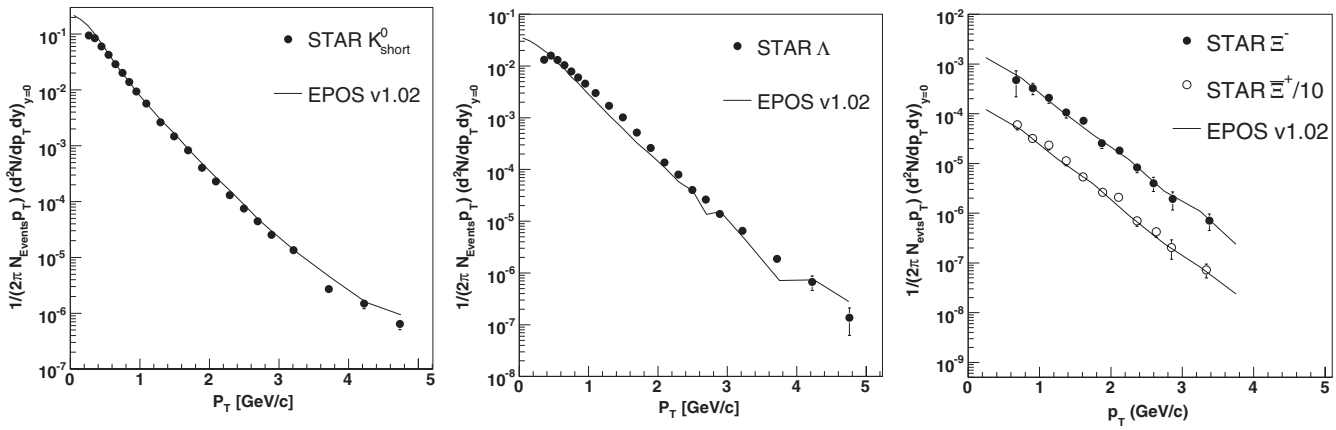

FIG. 19. Comparison of K^0_S, Λ, and Ξ^-, $\overline{\Xi}^+$ spectra with calculations from EPOS v1.02.

statistical nature of particle production observed in our data would be a simple reflection of the underlying statistical features of fragmentation. It is interesting to note that Biro and Mueller have shown that the folding of partonic power-law spectra can produce exponential spectral shapes of observed hadrons in the intermediate p_T region with no assumption of temperature or thermal equilibrium whatsoever [66].

Another possibly related idea is that of *phase space dominance* in which all possible final state configurations (i.e., those that are consistent with the energy, momentum, and quantum numbers of the initial state) are populated with equal probability [67]. The finite energy available in the collision allows many more final state configurations that contain low mass particles than those with high mass particles. The final state configurations containing high mass particles are therefore less likely to be observed, not because they are less probable, but because there are fewer of them relative to the low mass configurations.

We include in this section the results of a canonical statistical model fit, using THERMUS [68], to the STAR feed-down corrected ratios from $p + p$ collisions at $\sqrt{s} =$ 200 GeV. We used only the canonical formalism, as it has been determined from a microcanonical calculation that the volume of $p + p$ collision systems does not exceed 100 fm^3 [69]. Previous results have shown that such a small volume invalidates the use of a grand-canonical treatment [70]. The canonical calculation involves only the temperature T, baryon number B, charge Q, strangeness saturation factor γ_S, and the radius. For this fit, B and Q were both held fixed at 2.0. The resulting parameters are presented in Table XI and a graphical comparison is presented in Fig. 20.

TABLE XI. Comparison of a canonical fit to the STAR feed-down corrected ratios from $p + p$ collisions at $\sqrt{s} = 200$ GeV. The χ^2/ndf of the fit was $4.14/6 = 0.69$. See text for details.

	Canonical value
T	0.1680 ± 0.0081 GeV
B	2.000 (fixed)
Q	2.000 e (fixed)
γ_S	0.548 ± 0.052
Radius	3.83 ± 1.15 fm

The interpretation of the fit parameters is difficult in the context of a $p + p$ collision where the system is not expected to thermalize and the volume is small. It is important to note that in a pure thermal model, all emitted particles would be expected to reflect the same temperature. Nonthermal effects such as flow would modify this result. In $p + p$ collisions, the particle spectra clearly show different slopes, and those slopes are not in agreement with the T parameter that results from the statistical model fit to the particle ratios. As no flow is thought to be present in the $p + p$ system, this result is a further indication of contributions to the particle spectra from nonthermal processes.

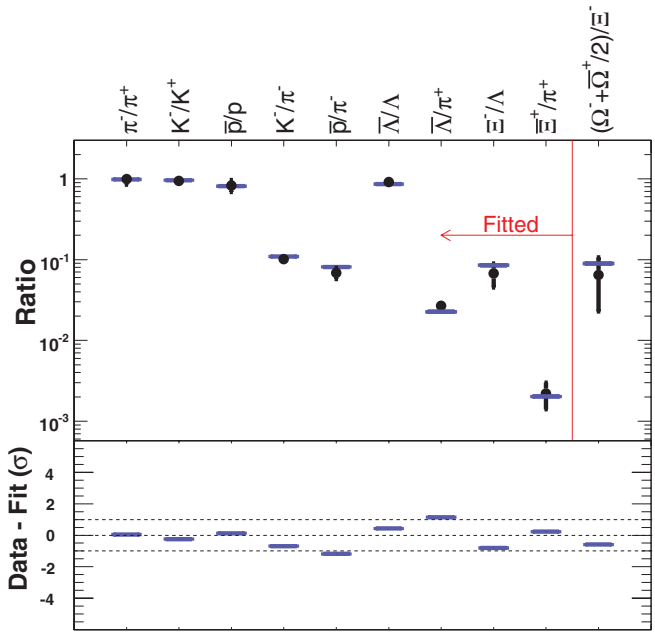

FIG. 20. (Color online) Parameters of ratio data to statistical model fit using THERMUS. Filled circles are ratios from $\sqrt{s} =$ 200 GeV collisions in STAR. Solid lines are the results from the statistical model fit. All ratios to the left of the vertical line were used in the fit. The $(\Omega^- + \overline{\Omega}^+/2)/\Xi^-$ ratio was then predicted from the fit results. Dashed lines in the lower panel are guides for the eye at 1σ.

VI. SUMMARY AND CONCLUSIONS

We have presented measurements of K^+, K^-, K^0_S, Λ, $\overline{\Lambda}$, Ξ^-, $\overline{\Xi}^+$, and $\Omega^- + \overline{\Omega}^+$ p_T spectra and midrapidity yields from $\sqrt{s} = 200$ GeV $p + p$ collisions in STAR. Corrections have been made for detector acceptance and efficiency as well as for the multiplicity dependence of the primary vertex finding and, in the case of the Λ and $\overline{\Lambda}$, feed down from higher mass weak decays. It was found that the measured range of transverse momentum necessitates a functional form that accounts for the power-law-like shape at high p_T. We have used a Lévy function to fit the spectra and extrapolate to low p_T.

The $\langle p_T \rangle$ and midrapidity yields are in excellent agreement for all species with previous measurements at the same energy but with greatly improved precision. The antiparticle to particle ratios are flat with p_T over the measured range for both the Λ and Ξ and therefore show no sign of quark-jet dominance at high p_T. The p_T integrated ratios approach unity with increasing strangeness content. The antibaryon to baryon ratios suggest that the midrapidity region at RHIC is almost baryon free, at least in $p + p$ collisions. The amount of deviation from unity expected from differing parton distribution functions must first be determined before any claim of significant baryon number transport from beam rapidity to midrapidity can be made.

We have demonstrated the scaling of transverse mass spectra for low p_T mesons and baryons onto a single curve to within 30% out to approximately 1.5 GeV in m_T. Above

2 GeV the m_T spectra show a clear difference in shape between mesons and baryons, with the mesons being harder than the baryons. This is the first observation of a difference between baryon and meson spectra in $p + p$ collisions and is mainly due to the high p_T (and therefore high m_T) coverage of the strange particles presented here. PYTHIA 6.3 seems to account for this effect and suggests it is mostly due to the dominance of gluon jets. More data are needed to determine the range of the effect.

The mean transverse momentum as a function of particle mass from both the $p + p$ and Au+Au systems has been compared. Both systems show a strong dependence of $\langle p_T \rangle$ on particle mass. It is also worth noting that the mass dependence of $\langle p_T \rangle$ in the $p + p$ system seems to be independent of collision energy, as the parametrization of the $\sqrt{s} = 25$ GeV ISR data seems to work well over the same range of measured masses at RHIC.

The dependence of $\langle p_T \rangle$ on event multiplicity was also studied for each of the three species (and antiparticles). The $\langle p_T \rangle$ shows a clear increase with event multiplicity for the K^0_S and Λ particles. There may be a mass ordering to the increase as the Λ baryons show a slightly faster increase with multiplicity than the K^0_S, but the present level of error on the Ξ data does not allow a definite statement to be made.

The multiplicity-binned K^0_S and Λ spectra show a clear correlation between high multiplicity events and the high p_T parts of the spectra. The spectral shapes for the K^0_S and Λ are observed to change with event multiplicity, and the Λ to K^0_S ratio increases over the lower p_T range and reaches higher values in the p_T range above $\sim$1.5 GeV/c for larger multiplicites. This suggests that the high multiplicity events produce more Λ hyperons relative to K^0_S than the low multiplicity events.

Comparisons of our spectra with PYTHIA v6.2 show only poor agreement at best without adjustment of the default parameters. In the relatively high p_T region (above 2 GeV/c) there is nearly an order of magnitude difference between our data and the model calculation. The more recent PYTHIA 6.3 provides a much better description of our K^0_S data, though a K factor of 3 is required to match the Λ and Ξ spectra as well as the observed rate of increase of $\langle p_T \rangle$ with multiplicity. NLO pQCD calculations with varied factorization scales are able to reproduce the high p_T shape of our K^0_S spectrum but not the Λ spectrum. Previous calculations at the same energy have been able to match the π^0 spectra almost perfectly, which suggests that there may be a mass dependence, a baryon-number dependence, or a strangeness dependence to the level of agreement achievable with pQCD.

The EPOS model has previously provided excellent descriptions of the π^-, K^-, and proton spectra from both $p + p$ and d + Au collisions measured by BRAHMS, PHENIX, and STAR at midrapidity and forward rapidity. We extended the comparison to strange and multistrange mesons and baryons and found the agreement between our data and the EPOS model to be at least as good as the best NLO calculations.

We have demonstrated the ability of the statistical model to fit our data to a reasonable degree with three parameters. Interpretation of the resulting parameters in the traditional fashion is not possible, as the $p + p$ colliding system is not considered to be thermalized. The T parameter does not agree with the slopes of the measured species, and we conclude that this result suggests a significant contribution of nonthermal processes to the particle spectra.

ACKNOWLEDGMENTS

We would like to thank S. Albino, P. Skands, W. Vogelsang, and K. Werner for several illuminating discussions and for the calculations they provided. We thank the RHIC Operations Group and RCF at BNL, and the NERSC Center at LBNL for their support. This work was supported in part by the HENP Divisions of the Office of Science of the US DOE; US NSF; BMBF of Germany; IN2P3, RA, RPL, and EMN of France; EPSRC of the United Kingdom; FAPESP of Brazil; Russian Ministry of Science and Technology; Ministry of Education and the NNSFC of China; IRP and GA of the Czech Republic; FOM of the Netherlands; DAE, DST, and CSIR of the Government of India; Swiss NSF; Polish State Committee for Scientific Research; STAA of Slovakia; and Korea Science & Engineering Foundation.

[1] G. Bocquet *et al.*, Phys. Lett. **B366**, 441 (1996).
[2] B. Alper *et al.* (British-Scandinavian Collaboration), Nucl. Phys. **B100**, 237 (1975).
[3] T. Alexopoulos *et al.* (E735 Collaboration), Phys. Rev. D **48**, 984 (1993).
[4] T. Alexopoulos *et al.* (E735 Collaboration), Phys. Lett. **B336**, 599 (1994).
[5] X. N. Wang and M. Gyulassy, Phys. Lett. **B282**, 466 (1992).
[6] K. H. Ackermann *et al.* (STAR Collaboration), Nucl. Instrum. Methods A **499**, 624 (2003).
[7] M. Anderson *et al.*, Nucl. Instrum. Methods A **499**, 659 (2003).
[8] H. Bichsel, Nucl. Instrum. Methods A **562**, 154 (2006); H. Bichsel, D. E. Groom, and S. R. Klein, J. Phys. G **33**, 258 (2006).
[9] J. Adams *et al.* (STAR Collaboration), Phys. Rev. Lett. **92**, 112301 (2004).
[10] J. Adams *et al.* (STAR Collaboration), Phys. Rev. C **70**, 041901 (2004).
[11] F. S. Bieser *et al.*, Nucl. Instrum. Methods A **499**, 766 (2003).
[12] C. Adler *et al.* (STAR Collaboration), Phys. Rev. Lett. **87**, 262302 (2001).
[13] C. Adler *et al.* (STAR Collaboration), Phys. Rev. Lett. **86**, 4778 (2001); **90**, 119903 (2003).
[14] R. E. Ansorge *et al.* (UA5 Collaboration), Nucl. Phys. **B328**, 36 (1989).
[15] R. E. Ansorge *et al.* (UA5 Collaboration), Phys. Lett. **B199**, 311 (1987).
[16] R. Hagedorn, Riv. Nuovo Cimento **6**, n. 10, 1 (1984).
[17] S. S. Adler *et al.* (PHENIX Collaboration), Phys. Rev. Lett. **91**, 241803 (2003).
[18] G. Wilk and Z. Włodarczyk, Phys. Rev. Lett. **84**, 2770 (2000).

[19] G. J. Alner *et al*. (UA5 Collaboration), Phys. Rep. **154**, 247 (1987).
[20] T. Sjöstrand *et al*., Comput. Phys. Commun. **135**, 238 (2001).
[21] B. Alper *et al*., Nucl. Phys. **B87**, 19 (1975).
[22] K. Alpgard *et al*., Phys. Lett. **B107**, 310 (1981).
[23] G. Gatoff and C. Y. Wong, Phys. Rev. D **46**, 997 (1992).
[24] J. Schaffner-Bielich, D. Kharzeev, L. McLerran, and R. Venugopalan, talk presented at Hirschegg 2002: Ultrarelativistic Heavy-Ion Collisions, Hirschegg, 13–19 Jan. 2002 (unpublished), arXiv:nucl-th/0202054.
[25] J. Schaffner-Bielich, D. Kharzeev, L. McLerran, and R. Venugopalan, Nucl. Phys. **A705**, 494 (2002).
[26] J. Adams *et al*. (STAR Collaboration), Phys. Rev. Lett. **92**, 112301 (2004).
[27] J. Adams *et al*. (STAR Collaboration), Phys. Lett. **B616**, 8 (2005).
[28] J. Adams *et al*. (STAR Collaboration), Phys. Lett. **B637**, 161 (2006).
[29] J. Harris, J. Phys. G **30**, S613 (2004).
[30] A. D. Martin, W. J. Stirling, and R. G. Roberts, Phys. Rev. D **50**, 6734 (1994).
[31] X. N. Wang, Phys. Rev. C **58**, 2321 (1998).
[32] M. Bourquin and J. M. Gaillard, Nucl. Phys. **B114**, 334 (1976).
[33] B. Alper *et al*., Nucl. Phys. **B114**, 1 (1976).
[34] J. W. Cronin *et al*. (Chicago-Princeton Group), Phys. Rev. D **11**, 3105 (1975).
[35] A. Dumitru and C. Spieles, Phys. Lett. **B446**, 326 (1999).
[36] X. N. Wang and M. Gyulassy, Phys. Rev. D **45**, 844 (1992).
[37] T. Sjöstrand, arXiv:hep-ph/9508391 (unpublished); B. Andersson, G. Gustafson, G. Ingelman, and T. Sjöstrand, Phys. Rep. **97**, 31 (1983).
[38] B. Andersson, *The Lund Model* (Cambridge University, Cambridge, England, 1998); B. Andersson *et al*., in Proceedings of the XXXVI Annual Winter School on Nuclear and Particle Physics, St. Petersburg, FL, 25 Feb. – 3 Mar. 2002 (unpublished), arXiv:hep-ph/0212122.
[39] R. D. Field, Phys. Rev. D **65**, 094006 (2002); R. D. Field, in Snowmass 2001 (unpublished), arXiv:hep-ph/0201192.
[40] R. Vogt, Heavy Ion Phys. **17**, 75 (2003).
[41] K. Eskola and H. Honkanen, Nucl. Phys. **A713**, 167 (2003).
[42] M. A. C. Lamont, J. Phys. G **30**, S963 (2004).
[43] B. A. Kniehl, G. Kramer, and B. Pötter, Nucl. Phys. **B597**, 337 (2001).
[44] D. deFlorian, M. Stratmann, and W. Vogelsang, Phys. Rev. D **57**, 5811 (1998).
[45] J. Adams *et al*. (STAR Collaboration), Phys. Rev. Lett. **92**, 171801 (2004).
[46] C. Bourrely and J. Soffer, Phys. Rev. D **68**, 014003 (2003).
[47] G. Abbiendi *et al*. (OPAL Collaboration), Eur. Phys. J. C **16**, 407 (2000).
[48] S. Albino, B. A. Kniehl, and G. Kramer, Nucl. Phys. **B725**, 181 (2005).
[49] X. Zhang, G. Fai, and P. Levai, Phys. Rev. Lett. **89**, 272301 (2002).
[50] J. Adams *et al*. (STAR Collaboration), Phys. Rev. Lett **97**, 152302 (2006).
[51] K. Werner, F. M. Liu, and T. Pierog, Phys. Rev. C **74**, 044902 (2006).
[52] K. Werner, F. M. Liu, and T. Pierog, J. Phys. G **31**, S985 (2005).
[53] R. Hagedorn, Nuovo Cimento Suppl. **3**, 147 (1965).
[54] R. Hagedorn and J. Randt, Nuovo Cimento Suppl. **6**, 169 (1968).
[55] R. Hagedorn, Nuovo Cimento Suppl. **6**, 311 (1968).
[56] R. Hagedorn, Nucl. Phys. **B24**, 93 (1970).
[57] P. J. Siemens and J. I. Kapusta, Phys. Rev. Lett. **43**, 1486 (1979).
[58] A. Z. Mekjian, Nucl. Phys. **A384**, 492 (1982).
[59] L. Csernai and J. Kapusta, Phys. Rep. **131**, 223 (1986).
[60] H. Stöcker and W. Greiner, Phys. Rep. **137**, 277 (1986).
[61] J. Cleymans and H. Satz, Z. Phys. C **57**, 135 (1993).
[62] J. Rafelski and J. Letessier, J. Phys. G **28**, 1819 (2002).
[63] P. Braun-Munzinger, K. Redlich, and J. Stachel, in *Quark-Gluon Plasma 3*, edited by R. C. Hwa and X.-N. Wang (World Scientific, Singapore, 2004).
[64] F. Becattini and U. Heinz, Z. Phys. C **76**, 269 (1997).
[65] F. Becattini, A. Giovannini, and S. Lupia, Z. Phys. C **72**, 491 (1996).
[66] T. Biro and B. Müller, Phys. Lett. **B578**, 78 (2004).
[67] J. Hormuzdiar, S. D. H. Hsu, and G. Mahlon, Int. J. Mod. Phys. E **12**, 649 (2003).
[68] S. Wheaton and J. Cleymans, arXiv:hep-ph/0407174 (unpublished).
[69] F. M. Liu, J. Aichelin, M. Bleicher, and K. Werner, Phys. Rev. C **69**, 054002 (2004).
[70] F. M. Liu, K. Werner, and J. Aichelin, Phys. Rev. C **68**, 024905 (2003).